

# A sample of 6C radio sources designed to find objects at redshift $> 4$ : III — imaging and the radio galaxy $K - z$ relation

Matt J. Jarvis<sup>1,2\*</sup>, Steve Rawlings<sup>1</sup>, Steve Eales<sup>3</sup>,  
 Katherine M. Blundell<sup>1</sup>, Andrew J. Bunker<sup>4,5</sup>, Steve Croft<sup>1</sup>,  
 Ross J. McLure<sup>1</sup>, Chris J. Willott<sup>1</sup>

<sup>1</sup> Astrophysics, Department of Physics, Keble Road, Oxford, OX1 3RH, U.K.

<sup>2</sup> Sterrewacht Leiden, Postbus 9513, 2300 RA Leiden, the Netherlands

<sup>3</sup> Department of Physics and Astronomy, University of Wales College of Cardiff, P.O. Box 913, Cardiff, CF2 3YB, UK

<sup>4</sup> Institute of Astronomy, University of Cambridge, Madingley Road, Cambridge CB3 0HA, U.K.

<sup>5</sup> Astronomy Department, University of California at Berkeley, CA 94720

1 February 2008

## ABSTRACT

In this paper, the third and final of a series, we present complete  $K$ –band imaging and some complementary  $I$ –band imaging of the filtered 6C\* sample. We find no systematic differences between the  $K - z$  relation of 6C\* radio galaxies and those from complete samples, so the near-infrared properties of luminous radio galaxies are not obviously biased by the additional 6C\* radio selection criteria (steep spectral index and small angular size). The 6C\*  $K - z$  data significantly improve delineation of the  $K - z$  relation for radio galaxies at high-redshift ( $z > 2$ ). Accounting for non-stellar contamination, and for correlations between radio luminosity and stellar mass, we find little support for previous claims that the underlying scatter in the stellar luminosity of radio galaxies increases significantly at  $z > 2$ . In a particular spatially-flat universe with a cosmological constant ( $\Omega_M = 0.3$  and  $\Omega_\Lambda = 0.7$ ), the most luminous radio sources appear to be associated with galaxies with a luminosity distribution with a high mean ( $\approx 5L^*$ ), and a low dispersion ( $\sigma \sim 0.5$  mag) which formed their stars at epochs corresponding to  $z \gtrsim 2.5$ . This result is in line with recent sub-mm studies of high-redshift radio galaxies and the inferred ages of extremely red objects from faint radio samples.

**Key words:** galaxies: active - galaxies: evolution - galaxies: formation

## 1 INTRODUCTION

The powerful radio galaxies and quasars we see in the local universe are almost exclusively associated with giant elliptical galaxies. Studies of these objects at high redshift have shown that the relationship between the near-infrared  $K$ -band and redshift  $z$  (known as the  $K - z$  diagram) is tight for the members of the 3CRR sample (Laing, Riley & Longair 1983) out to redshifts of  $z \sim 2$ . The tightness of this correlation was initially used to assert that the giant ellipticals hosting the low-

redshift ( $z < 0.6$ ) radio galaxies from the 3CRR sample are the result of passively-evolving stellar populations which formed at high-redshift (e.g. Lilly 1989).

Frequently, at higher redshifts ( $z > 0.6$ ) radio galaxies exhibit optical/infrared emission aligned with their radio axes. This aligned emission is not expected if the host galaxy emission is a consequence of an old stellar population alone. The mechanism which causes this ‘alignment effect’ has been the subject of much debate over the past decade. Different possibilities include, incorporating jet driven star bursts (e.g. McCarthy et al. 1987; Chambers, Miley & van Breugel 1987), scattered quasar light (e.g. Tadhunter et al. 1987) and emis-

\* Email:jarvis@strw.leidenuniv.nl

sion from inverse Compton scattering of the cosmic microwave background (e.g. Daly et al. 1992) have all been put forward as possible explanations. A combination of the three mechanisms mentioned above, as well as others, may explain the alignment effect in the majority of sources.

Dunlop & Peacock (1993) using 3CRR sources along with fainter Parkes radio galaxies found that this alignment effect is weaker in the near-infrared than in the optical, indicating that the aligned component is blue in colour. They also found that the alignment was a strong function of radio luminosity at  $z \sim 1$ , with the most luminous sources exhibiting a greater degree of alignment.

Best, Longair & Röttgering (1997, 1998) and McLure & Dunlop (2000) both find that the hosts of 3CRR radio galaxies at  $z \sim 1$  are consistent with massive evolved ellipticals, whose infrared emission is dominated by starlight. McLure & Dunlop also demonstrate that the hosts of 3CRR radio galaxies at  $z \sim 1$  are essentially the same as the hosts of 3CRR radio galaxies at  $z \sim 0.2$ . The small amount of passive evolution between  $z \sim 1$  and  $z \sim 0.2$  implies a high-formation redshift ( $z > 3$ ), within most reasonable cosmologies, for these massive elliptical host galaxies.

Eales et al. (1997) using the 3CRR sample and the fainter 6CE sample (Eales 1985; Rawlings, Eales & Lacy 2001) found that lower luminosity radio sources are associated with optically fainter host galaxies. This led Eales et al. (1997) to conclude that a correlation exists between the radio luminosity and optical/infrared luminosity.

Another factor which is dependent on radio luminosity and contributes to the optical/infrared emission is the contamination from bright emission lines which have been redshifted into the  $K$ -band window (e.g. Eales & Rawlings 1993). This contamination from emission lines means that the stellar population is not the only contributor to the  $K$ -band flux. It is now well documented that the emission-line strength in radio galaxies is intrinsically linked to the strength of the underlying quasar continuum and thus the radio emission (e.g. Rawlings & Saunders 1991; Willott et al. 1999; Jarvis et al. 2001). Therefore, due to the biases inherent in a single flux-density-limited sample such as 3CRR (e.g. Blundell, Rawlings & Willott 1999), the most distant sources are always the most luminous, which in turn produce the strongest emission lines. At low-redshift this contamination is negligible. However, at  $z > 1$  the effect becomes increasingly important, as the bright optical emission lines are redshifted into the near-infrared. With fainter samples such as 6CE, this effect has, to a certain degree been quashed due to the low-luminosities compared to 3CRR. However, at  $z > 2$  the luminosities of these sources are similar to the 3CRR sources at  $z \sim 0.5$ , thus the emission-line contributions need to be

considered. These effects may thus have an important effect on the  $K - z$  diagram at high redshift.

Eales et al. (1997) also conclude that at redshifts  $z > 2$  we are beginning to see the formation epoch of these massive ellipticals. The relative brightness of the 6CE sources at  $z > 2$  in comparison to a passively-evolving stellar population, and also the higher dispersion in the  $K$ -band magnitudes at high redshift both point to this explanation. However, the relatively low number of sources above  $z > 2$  in the 6CE sample place considerable uncertainties on this high-redshift behaviour.

In this paper we present our  $K$ -band imaging data for all sources in the 6C\* sample. The 6C\* sample is a filtered sample, aimed at finding radio galaxies at  $z > 4$ . The filtering criteria employed are based on the radio properties of the sources, namely steep-spectral index ( $\alpha \geq 0.981^\dagger$ ) and small angular size ( $\theta < 15$  arcsec). A detailed description of the sample selection and filtering criteria is given in Blundell et al. (1998; paper I). The spectrophotometric observations are presented in (Jarvis et al. 2001; paper II). We are now able to use this filtered sample, along with the 6CE sample (Eales 1985; Rawlings et al. 2001), and the high-redshift sources from the 7C-III sample of Lacy, Bunker & Ridgway (2000) to investigate the stellar continuum of high-redshift radio galaxies with the  $K - z$  Hubble diagram up to  $z \approx 4.4$ .

In Sec. 2 we outline the observing and reduction procedures for our  $K$ -band imaging data. We also present  $K$ -band images for 28 of the 29 sources in the final 6C\* sample with their radio contours overlaid. A full discussion and images of the other member of the 6C\* sample, 6C\*0140+326, which is at  $z = 4.41$  may be found in Rawlings et al. (1996). In Sec. 3 we provide brief notes of each source in the sample. We investigate the shape and properties of the  $K - z$  Hubble diagram to  $z \approx 4.4$  in Sec. 4, and in Sec. 5 we suggest an evolutionary scenario to explain this diagram. We summarise our conclusions in Sec. 6. We also present  $I$ -band images of some of the 6C\* sources in Appendix A, and imaging data on the sources no longer deemed to be members of 6C\* in Appendix B. For consistency with previous papers we use  $H_0 = 50 \text{ km s}^{-1} \text{ Mpc}^{-1}$ , in a spatially flat cosmology with  $\Omega_M = 1$  and  $\Omega_\Lambda = 0$ , unless otherwise stated.

## 2 $K$ -band IMAGING

### 2.1 Observations

The  $K$ -band ( $2.2\mu\text{m}$ ) imaging of the 6C\* sample was made over several observing runs at the United Kingdom Infrared Telescope (UKIRT), beginning in 1993,

<sup>†</sup> We use the convention for spectral index  $S_\nu \propto \nu^{-\alpha}$ , where  $\alpha$  is measured between observed 151 MHz and 4.9 GHz.

with the most recent observations made in September 2000. The earliest observations (1993 - 1994) were all made using the IRCAM near-infrared camera, which consists of a  $58 \times 62$  element infrared array, with a pixel scale of  $0.62 \text{ arcsec pixel}^{-1}$ . For the second observing run in 1997, IRCAM-3 was used. IRCAM-3 is a InSb  $256 \times 256$  array with a pixel scale of  $0.286 \text{ arcsec pixel}^{-1}$  and field of view  $73 \times 73 \text{ arcsec}^2$ . The most recent observations were made using the new infrared camera on UKIRT, UFTI (UKIRT Fast-Track Imager), which comprises a  $1024 \times 1024$  HgCdTe array, with a plate scale of  $0.091 \text{ arcsec pixel}^{-1}$ , giving a field of view of  $92 \times 92 \text{ arcsec}^2$ . All observations were made in photometric conditions unless stated otherwise, with the typical seeing spanning  $0.6 - 1.2 \text{ arcsec}$ . From 1997 onwards, the tip-tilt system on UKIRT was utilised to give sub-arcsec imaging on all observations.

In order to subtract the rapidly changing sky background at these wavelengths, to provide a good flat-field and to minimise the effects of cosmic ray contamination and bad pixels, we used the standard observing strategy of offsetting the position of the telescope by e.g.  $8 \text{ arcsec}$  between each exposure. The offsets were arranged in a  $3 \times 3$  mosaic of nine exposures. The integration time varies between objects in the sample, due to time constraints and also based on the magnitude of the source. A summary of all the  $K$ -band observations is given in Table 1.

## 2.2 Data reduction

The  $K$ -band images were reduced using standard procedures. We first subtracted the dark current from each image. We then divided by the normalised flat-field, created by combining the nine exposures of the particular field with a median filter, which removes any objects which appear in different positions on the chip over the nine exposures. To combine the individual images we registered all of the frames using a bright star which was present in each of the nine pointings. In the cases where there was no bright star in the images, the offsets recorded in the image headers were used to align the frames. The registered images were then combined using an average clipping procedure to reject pixels more than  $4\sigma$  away from the median of the distribution.

Astrometry for each image was achieved by identifying sources in the image with objects in the APM catalogue<sup>‡</sup>. In the few cases where the APM did not cover the sky area required, ground-based images with accurately determined astrometry were used, and in one case (6C\*0133+486) the Digitised Sky Survey (DSS) was used. In the majority of the cases we were able to identify three or more sources on our images with

objects on the finding charts, and in these cases the astrometry (performed with the IRAF task **gasp**) is accurate to  $\lesssim 1 \text{ arcsec}$ . In the cases where three or more objects could not be identified with objects on the finding charts, astrometric scaling from the previous images was used to perform the astrometry on the images from a single securely identified object. The reduced images are shown in Fig. 1 with the radio contours overlaid.

## 3 NOTES ON INDIVIDUAL SOURCES

**6C\*0020+440** ( $z = 2.988$ ) The extremely faint plausible ID, (a) in Fig. 1, is situated between the two radio lobes but closer to the eastern lobe. There are also two bright objects close to the radio structure. Both object (b)  $\approx 2.5 \text{ arcsec}$  to the north of our ID, and object (c)  $\approx 3 \text{ arcsec}$  to the south-west of this identification may contribute some flux to the  $K$ -band magnitude in apertures  $> 3 \text{ arcsec}$ .

**6C\*0024+356** ( $z = 2.161$ ) The ID of this source lies between the two radio lobes but shifted towards the western lobe. The ID is close to a brighter object making any magnitude estimation difficult.

**6C\*0031+403** ( $z = 1.619$ ) Our  $K$ -band image shows a bright ID co-spatial with the flat-spectrum core. The radio structure of this source is somewhat unusual for the 6C\* sample: a one-sided jet emerges from the bright core, suggestive of a jet disrupted on one side of the source. We speculate that this object might be a reddened quasar with an additional non-stellar component to the  $K$ -band light, due to the unusually bright  $K$ -band magnitude for a source at this redshift, although there is no evidence of any broad line component from our spectroscopic observations.

**6C\*0032+412** ( $z = 3.658$ ) Our infrared spectroscopic observations of this source (Jarvis et al. 2001) reveals that  $\sim 50\%$  of the  $K$ -band flux is contributed by the [OIII] emission lines at  $4959 \text{ \AA}$  and  $5007 \text{ \AA}$ . The errors on this value are large because of the tentative nature of the UKIRT ID, and consequently inaccurate photometry. There are hints that the  $K$ -band light is extended along the radio axis, probably due to significant contamination by emission lines. The astrometry for this image is accurate to  $\sim 1.5 \text{ arcsec}$  and uncertain enough to reconcile the apparent displacement of the  $K$ -band ID with the radio emission.

**6C\*0041+469** ( $z = 2.14?$ ) Our  $I$ -band (see appendix A) and  $K$ -band images reveal highly aligned emission, although the astrometry for the  $I$ -band image is offset from the expected position by  $\sim 1 \text{ arcsec}$  to the west with our astrometric fit to the image. The tentative redshift of this object is  $z = 2.14$ ; at this redshift the  $H\alpha$  emission line is redshifted into the  $K$ -band window and thus there may be a non-stellar component

<sup>‡</sup> For more details see <http://www.ast.cam.ac.uk/~apmcat/>

Source name	Instrument	Date	Exposure time / s
6C*0020+440	<b>IRCAM</b>	<b>94Jan16</b>	<b>1440</b>
6C*0024+356	<b>IRCAM-3</b>	<b>97Dec13</b>	<b>540</b>
6C*0031+403	<b>IRCAM</b>	<b>94Jan18</b>	<b>1260</b>
6C*0032+412	<b>IRCAM</b>	<b>93Jan10</b>	<b>3240</b>
6C*0041+469	<b>IRCAM</b>	<b>94Jan16</b>	<b>1440</b>
	IRCAM-3	97Dec13	540
6C*0050+419	IRCAM	94Jan18	1260
	<b>IRCAM-3</b>	<b>97Dec13</b>	<b>540</b>
	UFTI	00Sep25	960
6C*0052+471	<b>IRCAM</b>	<b>94Jan18</b>	<b>630</b>
6C*0058+495	<b>IRCAM</b>	<b>94Jan16</b>	<b>1440</b>
6C*0106+397	IRCAM-3	97Dec13	540
	UFTI	00Sep25	960
6C*0112+372	<b>UFTI</b>	<b>00Jul28</b>	<b>540</b>
6C*0115+394	<b>IRCAM-3</b>	<b>97Dec13</b>	<b>540</b>
6C*0118+486	IRCAM	94Jan16	1440
	UFTI	<b>00Jul28</b>	<b>540</b>
6C*0122+426	<b>IRCAM-3</b>	<b>97Dec13</b>	<b>540</b>
6C*0128+394	<b>IRCAM</b>	<b>94Jan18</b>	<b>1260</b>
6C*0132+330	<b>IRCAM-3</b>	<b>97Dec13</b>	<b>540</b>
6C*0133+486	<b>IRCAM-3</b>	<b>97Dec13</b>	<b>540</b>
6C*0135+313	<b>IRCAM-3</b>	<b>97Dec13</b>	<b>540</b>
6C*0136+388	<b>IRCAM</b>	<b>94Jan16</b>	<b>1440</b>
6C*0139+344	IRCAM	94Jan18	630
	<b>IRCAM-3</b>	<b>97Dec13</b>	<b>540</b>
6C*0142+427	<b>IRCAM</b>	<b>94Jan16</b>	<b>1440</b>
6C*0152+463	IRCAM	94Jan16	1440
	<b>IRCAM-3</b>	<b>97Dec13</b>	<b>540</b>
6C*0154+450	<b>IRCAM-3</b>	<b>97Dec13</b>	<b>540</b>
6C*0155+424	IRCAM	94Jan18	630
	<b>IRCAM-3</b>	<b>97Dec13</b>	<b>540</b>
6C*0158+315	IRCAM	94Jan17	1260
	<b>IRCAM-3</b>	<b>97Dec13</b>	<b>540</b>
6C*0201+499	<b>IRCAM</b>	<b>94Jan18</b>	<b>1260</b>
	IRCAM-3	97Dec13	540
6C*0202+478	<b>IRCAM</b>	<b>94Jan18</b>	<b>1260</b>
6C*0208+344	<b>IRCAM</b>	<b>94Jan17</b>	<b>1440</b>
	IRCAM-3	97Dec13	540
6C*0209+276	<b>IRCAM</b>	<b>94Jan17</b>	<b>1620</b>

Table 1: Log of the *K*-band imaging observations of the sources present in the 6C\* sample. The imaging data on the  $z = 4.41$  radio galaxy, 6C\*0140+326 is presented in Rawlings et al. (1996). The bold lettering indicates the images shown in Fig. 1. The Sep00 image of 6C\*0050+419 is not of sufficient depth to detect the object in *K*-band, due to non-photometric conditions, therefore we use the Dec97 image for our analysis.

contributing to the *K*-band flux, however, the *K*-band magnitude is consistent with the quoted redshift.

**6C\*0050+419** ( $z = 1.748?$ ) There is a faint object to the south of the peak of the compact radio emission

(a), which is most plausibly the ID. Deep *I*-band imaging with the Keck telescope (appendix A) also reveals a faint blob of emission to the south of the peak of the radio emission. There also appears to be a faint blob

Source	Magnitude from 3" diameter	Magnitude from 5" diameter	Magnitude from 8" diameter	$z$	Detector	Radio frequency
6C*0020+440	19.94 ± 0.41	18.90 ± 0.27	nbo	2.988	IRCAM	8.9 GHz
6C*0024+356	18.51 ± 0.12	nbo	nbo	2.161	IRCAM-3	8.4 GHz
6C*0031+403	17.68 ± 0.05	17.12 ± 0.06	16.80 ± 0.08	1.619	IRCAM	1.5 GHz
6C*0032+412	19.95 ± 0.43	19.62 ± 0.42	19.57 ± 0.55	3.658	IRCAM	4.9 GHz
6C*0041+469	19.36 ± 0.17	19.18 ± 0.27	19.19 ± 0.51	2.140?	IRCAM	4.9 GHz
	20.13 ± 0.62	19.65 ± 0.73	19.32 ± 0.96	2.140	IRCAM-3	
6C*0050+419	20.42 ± 0.53	20.39 ± 0.93	19.61 ± 1.35	1.748?	IRCAM	
	19.66 ± 0.37	19.43 ± 0.70	18.80 ± 0.54	1.748?	IRCAM-3	8.4 GHz
6C*0052+471	18.01 ± 0.10	17.89 ± 0.15	17.83 ± 0.27	1.935	IRCAM	8.4 GHz
6C*0058+495	18.02 ± 0.06	17.73 ± 0.08	17.62 ± 0.14	1.173	IRCAM	4.9 GHz
6C*0106+397	19.25 ± 0.39	18.78 ± 0.36	18.43 ± 0.41	2.284	IRCAM-3	1.5 GHz
6C*0112+372	18.25 ± 0.05	18.12 ± 0.08	17.97 ± 0.13	2.535	UFTI	4.9 GHz
6C*0115+394	18.88 ± 0.19	18.74 ± 0.30	18.58 ± 0.47	2.241	IRCAM-3	8.4 GHz
6C*0118+486	18.58 ± 0.09	18.28 ± 0.12	18.13 ± 0.20	2.350	IRCAM	
	18.49 ± 0.07	18.23 ± 0.10	18.31 ± 0.20	2.350	UFTI	8.4 GHz
6C*0122+426	18.91 ± 0.19	18.88 ± 0.31	18.72 ± 0.35	2.635	IRCAM-3	8.4 GHz
6C*0128+394	18.01 ± 0.07	17.78 ± 0.11	17.72 ± 0.22	0.929	IRCAM	8.4 GHz
6C*0132+330	19.30 ± 0.27	18.80 ± 0.29	18.81 ± 0.52	1.710	IRCAM-3	8.4 GHz
6C*0133+486	18.72 ± 0.16	18.69 ± 0.27	nbo	1.029?	IRCAM-3	8.4 GHz
6C*0135+313	19.92 ± 0.59	19.47 ± 0.55	nbo	2.199	IRCAM-3	1.5 GHz
6C*0136+388	18.07 ± 0.05	17.57 ± 0.05	17.32 ± 0.08	1.108?	IRCAM	4.9 GHz
6C*0139+344	18.17 ± 0.09	nbo	nbo	1.637	IRCAM	
	18.40 ± 0.11	nbo	nbo	1.637	IRCAM-3	4.9 GHz
6C*0142+427	19.18 ± 0.17	18.81 ± 0.22	18.75 ± 0.53	2.225	IRCAM	1.5 GHz
6C*0152+463	19.04 ± 0.15	18.87 ± 0.23	18.99 ± 0.49	2.279	IRCAM	
	19.24 ± 0.27	18.55 ± 0.25	18.40 ± 0.39	2.279	IRCAM-3	4.9 GHz
6C*0154+450	17.06 ± 0.04	17.03 ± 0.06	16.99 ± 0.11	1.295	IRCAM-3	8.4 GHz
6C*0155+424S	17.47 ± 0.05	17.17 ± 0.07	nbo	0.513	IRCAM	
	17.62 ± 0.06	17.38 ± 0.08	nbo	0.513	IRCAM-3	8.4 GHz
6C*0158+315	18.65 ± 0.12	18.21 ± 0.14	17.91 ± 0.19	1.505	IRCAM	
	18.82 ± 0.16	18.53 ± 0.21	18.17 ± 0.27	1.505	IRCAM-3	4.9 GHz
6C*0201+499	18.76 ± 0.11	18.66 ± 0.18	18.50 ± 0.29	1.981	IRCAM	4.9 GHz
	19.27 ± 0.52	19.20 ± 0.42	18.68 ± 0.48	1.981	IRCAM-3	
6C*0202+478	18.90 ± 0.80	nbo	nbo	1.613?	IRCAM	8.4 GHz
6C*0208+344	19.26 ± 0.21	19.03 ± 0.33	18.99 ± 0.95	1.920	IRCAM	4.9 GHz
	19.62 ± 0.34	19.16 ± 0.41	19.05 ± 0.53	1.920	IRCAM-3	
6C*0209+276	18.66 ± 0.09	18.28 ± 0.12	18.10 ± 0.18	1.141?	IRCAM	4.9 GHz

Table 2:  $K$ -band magnitudes for the 6C\* sample in three different angular apertures. The redshifts are the spectroscopic redshifts from Jarvis et al. (2001). ‘nbo’ denotes that the radio galaxy was too close to a nearby object to measure the magnitude reliably. The  $K$ -band magnitude for 6C\*0050+419 is for object ‘a’ in Fig. 1. The  $K$ -band magnitude of 6C\*0139+344 may have a contribution to the  $K$ -band flux from a foreground galaxy. Column 7 gives the frequency of the radio maps shown in Fig. 1. The  $K$ -band magnitude for 6C\*0202+478 is an estimate, because of its close proximity to other nearby objects.

of emission slightly to the north of the radio peak in the  $I$ -band image, although there is no visible  $K$ -band counterpart we cannot rule this out as being associated with the radio source. There is also a faint blob to the south-west (object ‘b’) in both our  $K$ - and  $I$ -band images co-spatial with the faint radio component in our 8.4 GHz map, which could also be the ID, and has a  $K$ -band magnitude of  $K \simeq 19.5$  (8 arcsec aperture).

**6C\*0052+471** ( $z = 1.935$ ) We find bright, unresolved  $K$ -band emission associated with the centre of the radio emission; the object is a quasar.

**6C\*0058+495** ( $z = 1.173$ ) A bright  $K$ -band ID is co-spatial (within the astrometric uncertainty) with the centre of the radio lobes, although no core component is present in our radio maps.

**6C\*0106+397** ( $z = 2.284$ ) We find faint  $K$ -band emission situated between the two radio lobes, and we take this as the ID. There is much brighter emission to the south-east of the southern most radio lobe with  $K = 17.8$  (8 arcsec aperture) which we associate with a  $z = 0.632$  foreground galaxy (Jarvis et al. 2001).

(1)	(2)	(3)	(4)	(5)	(6)	(7)	(8)	(9)	(10)	(11)
Source	$S_{151}$	$\alpha_{151}$	$z$	$K$	$R$	$\log_{10} L_{151}$	Line	$\log_{10} L_{\text{line}}$	Class	Ref
6C*0020+440	2.00	0.97	2.988	18.90 (5)		28.03	Ly $\alpha$	36.37	HEG	Jea
6C*0024+356	1.09	0.69	2.161	18.51 (3)	22.80	27.33	Ly $\alpha$	35.96	LEG?	Jea
6C*0031+403	0.96	0.90	1.618	16.80 (8)	22.42	27.08	CIV	35.18	HEG?	Jea
6C*0032+412	1.29	1.28	3.658	19.57 (8)		28.21	Ly $\alpha$	36.35	HEG	Jea
6C*0041+469	1.53	0.61	2.145?	19.19 (8)		27.31	Ly $\alpha$	35.55	HEG?	Jea
6C*0050+419	1.00	1.24	1.748?	18.80 (8)		27.31	HeII?	34.16	HEG?	Jea
6C*0052+471	1.31	0.88	1.935	17.83 (8)		27.38	Ly $\alpha$	36.12	Q	Jea
6C*0058+495	0.97	0.74	1.173	17.62 (8)		26.74	[OII]	35.92	HEG	Jea
6C*0106+397	0.96	0.52	2.284	18.43 (8)		27.25	CIV	34.87	HEG	Jea
6C*0112+372	1.03	0.42	2.535	17.97 (8)		27.36	Ly $\alpha$	37.05	HEG	Jea
6C*0115+394	0.96	1.06	2.241	18.58 (8)	22.31	27.48	Ly $\alpha$	37.15	HEG	Jea
6C*0118+486	0.98	1.47	2.350	18.13 (8)		27.70	Ly $\alpha$	36.17	HEG	Jea
6C*0122+426	1.05	0.53	2.635	18.88 (5)	23.10	27.43	Ly $\alpha$	35.97	HEG	Jea
6C*0128+394	1.94	0.50	0.929	17.72 (8)		26.75	[OII]	34.52	HEG?	Jea
6C*0132+330	1.56	1.28	1.710	18.81 (8)	22.12	27.50	CIII]	35.19	HEG	Jea
6C*0133+486	1.89	1.22	1.029?	18.69 (5)	23.39	27.04	[OII]?	35.05	LEG?	Jea
6C*0135+313	1.24	1.18	2.199	19.47 (5)	23.82	27.62	Ly $\alpha$	37.71	HEG	Jea
6C*0136+388	0.99	0.68	1.108?	17.32 (8)	22.60	26.68	[OII]?	35.68	LEG?	Jea
6C*0139+344	1.10	0.74	1.637	18.40 (3)		27.11	[OII]	—	HEG	Jea
6C*0140+326	1.00	0.62	4.410	20.00 $^{\dagger}$ (2)		27.94	Ly $\alpha$	36.87	HEG	Rea
6C*0142+427	1.46	1.20	2.225	18.75 (8)		27.70	Ly $\alpha$	36.72	HEG	Jea
6C*0152+463	1.29	0.79	2.279	18.40 (8)		27.49	Ly $\alpha$	36.15	LEG?	Jea
6C*0154+450	1.15	1.28	1.295	16.99 (8)		27.07	CIV	37.22	Q	Jea
6C*0155+424	1.51	0.89	0.513	17.38 (5)	20.76	26.20	[OII]	34.66	LEG?	Jea
6C*0158+315	1.51	0.75	1.505	17.91 (8)	22.28	27.16	MgII	36.31	HEG?	Jea
6C*0201+499	1.14	0.74	1.981	18.50 (8)		27.30	Ly $\alpha$	35.75	HEG	Jea
6C*0202+478	1.06	0.86	1.620?	18.90 $^{\ddagger}$ (3)		27.13	CII]?	36.10	HEG?	Jea
6C*0208+344	0.97	0.57	1.920	19.03 (5)		27.13	Ly $\alpha$	36.01	HEG	Jea
6C*0209+476	1.14	0.69	1.141?	18.10 (8)		26.77	[OII]?	35.18	LEG?	Jea
<b>Excluded sources</b>										
6C*0100+312	1.16	1.68	1.189	16.54 (8)	—	27.14	MgII	36.14	Q	Jea
6C*0107+448	1.04	1.42	1.301?	—	—	27.09	[OII]?	34.82	G	Jea
6C*0111+367	1.11	—	—	17.80 (8)	—	—	—	—	G	Jea
6C*0120+329	1.87	1.48	0.0164	—	—	23.24	—	—	G	deR
6C*0141+425	1.64	1.06	0.0508	—	—	24.16	abs	—	G	Jea

Table 3: Summary of the observational data on the 6C\* sample (an ascii version of this table along with other information about the 6C\* sample can also be found at <http://www.strw.leidenuniv.nl/~jarvis/6cs/>). **Column 1:** Name of the 6C\* source. **Column 2:** 151 MHz flux-density measurements in Jy from the 6C survey (Hales et al. 1993). **Column 3:** radio spectral index evaluated at rest-frame 151 MHz using the polynomial fit described in Blundell et al. (1998). **Column 4:** redshift, ‘?’ signifies that this value is uncertain. **Column 5:**  $K$ -band magnitudes within the angular aperture in arcseconds given in brackets.  $\dagger$  signifies that the measurement is from van Breugel et al. (1998) and is a  $K'$  magnitude,  $\ddagger$  signifies that the optical ID is too close to a nearby object to measure the  $K$ -band magnitude with any accuracy. **Column 6:**  $R$ -band magnitude where available (Jarvis 2000), measured using the same aperture as that for the  $K$ -band magnitude. **Column 7:**  $\log_{10}$  of the rest-frame 151 MHz radio luminosity (measured in units of  $\text{W Hz}^{-1} \text{ sr}^{-1}$ ), calculated using the polynomial fit to the radio spectra for  $\Omega_M = 1, \Omega_\Lambda = 0, H_0 = 50 \text{ km s}^{-1} \text{ Mpc}^{-1}$ . **Column 8:** Prominent emission line in the existing spectra, ‘?’ signifies that the line identification is uncertain. **Column 9:**  $\log_{10}$  of the luminosity of the line listed in Column 8 (measured in units of W), for  $\Omega_M = 1, \Omega_\Lambda = 0$  and  $H_0 = 50 \text{ km s}^{-1} \text{ Mpc}^{-1}$ . ‘-’ signifies that the data were inadequate to obtain a line luminosity through the absence of a spectrophotometric standard. **Column 10:** classification, Q=quasar, HEG=high-excitation galaxy, LEG=low-excitation galaxy, following the prescription of Rawlings et al. (2001), i.e. using the detection of any line from at least a doubly-ionised ion and G=galaxy for which we have little or no spectroscopic information to classify it as HEG or LEG but one which is spatially resolved in our imaging data. **Column 11:** The reference to the redshift of the source, Jea - Jarvis et al. (2001); Rea - Rawlings et al. (1996); and deR - de Ruiter et al. (1986).

**6C\*0112+372** ( $z = 2.535$ ) This source is spatially resolved in 0.9 arcsec seeing at the position of the bright radio emission, and is therefore identified as a radio galaxy. The peak of the radio emission is represented by the white cross in Fig. 1.

**6C\*0115+394** ( $z = 2.241$ ) Our  $K$ -band image shows a resolved identification in 0.8 arcsec seeing, co-spatial with the radio core.

**6C\*0118+386** ( $z = 2.350$ ) The identification of this source is coincident with the central radio component which has a spectral index of  $\alpha \sim 0.5$ , and is taken to be the site of the AGN. The  $K$ -band magnitude of this object is not unreasonable for the redshift, but we cannot eliminate the possibility that it is contaminated by a foreground  $z = 0.529$  galaxy seen in emission lines in the spectrum. This galaxy is sufficiently far from either of the radio lobes that significant gravitational lensing of the flux-density appears unlikely. We note three bright resolved galaxies near the northern hotspot which may be part of an intervening  $z = 0.529$  group or cluster.

**6C\*0122+426** ( $z = 2.635$ ) Our  $K$ -band image shows faint emission associated with the radio source. Our astrometry is not good enough to determine whether the ID is on either of the bright radio components or between them.

**6C\*0128+394** ( $z = 0.929$ ) Our  $K$ -band image shows a bright ID coincident with the centre of the double lobed radio emission.

**6C\*0132+330** ( $z = 1.710$ ) We find a very faint  $K$ -band ID associated with the centroid of the radio emission.

**6C\*0133+486** ( $z = 1.029?$ ) There are two possible identifications for this radio source, although these are along the line of the radio jet and both may be associated with the radio galaxy. Our tentative redshift of  $z = 1.029$  from the brightest component (a) leads us to conclude, from the  $K - z$  diagram, that this is the host galaxy, although this is still  $\sim 0.8$  magnitudes fainter than the best-fit line through the 6CE/6C\*  $K - z$  diagram (Fig. 3). However, object (b)  $\sim 2$  arcsec to the north cannot be ruled out as the host and further spectroscopic observations will be needed to confirm the ID and redshift of this radio source.

**6C\*0135+313** ( $z = 2.199$ ) The  $K$ -band ID of this source lies at the centre of the bright radio emission. There is also a brighter source ( $K = 18.9$  in an 8 arcsec aperture) to the south-east which is possibly a foreground object, although we have no spectroscopic data to confirm this.

**6C\*0136+388** ( $z = 1.108?$ ) The  $K$ -band ID of this source lies at the radio core. The radio core is not visible in the image presented in Fig. 1 because of the bright  $K$ -band ID; the peak in the radio emission is represented by the white cross. The  $K$ -band magnitude is also consistent with the  $K - z$  relation at this redshift.

**6C\*0139+344** ( $z = 1.637$ ) Our optical spectra reveal a nearby foreground galaxy at  $z = 0.37$  which could be contributing to our measured  $K$ -band magnitude. Our  $K$ -band image reveals two galaxies towards what appears to be a steep-spectrum radio lobe to the north. We take the fainter of these (a) to be the radio galaxy with the  $z = 0.37$  foreground galaxy (b) approximately 2.5 arcsec to the north, which is in agreement with our astrometry from the 2D spectrum. There are no objects in our images which are coincident with the faint radio component in our 4.9 GHz map at 01 39 25.87 +34 27 02.5 (B1950) which we originally thought to be the core.

**6C\*0140+326** ( $z = 4.41$ ) This gravitationally lensed source is discussed in detail in Rawlings et al. (1996).

**6C\*0142+427** ( $z = 2.225$ ) The  $K$ -band ID for this source is coincident with the radio core.

**6C\*0152+463** ( $z = 2.279$ ) The  $K$ -band ID of this source lies between the two radio lobes.

**6C\*0154+450** ( $z = 1.295$ ) We find an unresolved point source co-spatial with the radio core, as expected for a quasar.

**6C\*0155+424** ( $z = 0.513$ ) The  $R-$  (Jarvis 2000) and  $K$ -band images of this radio source reveal three optically bright sources that could each plausibly be the radio galaxy. The  $K$ -band magnitudes of all three point towards a low redshift ( $z < 1$ ) and our optical spectroscopy revealed that the ID closest to the centre of the radio emission has a redshift  $z = 0.513$  and is probably the host galaxy on positional grounds. The nearest neighbour to this source is  $\lesssim 1.5$  arcsec to the north-west, and the similar  $K$ -band magnitudes suggest that these two objects could be in the process of merging. There is also another optical source  $\approx 4$  arcsec to the south-east of these two objects. This also has a similarly bright  $K$ -band magnitude and is also plausibly a true companion galaxy. There is faint diffuse emission surrounding the two closest objects, and the third has faint emission reaching towards the other two, which is also indicative that this system may be undergoing a major merger. Further spectroscopy in good seeing will be required to ascertain whether they are merging, and deeper imaging may find more diffuse emission surrounding all three objects within the radio emission.

**6C\*0158+315** ( $z = 1.505$ ) We find a  $K$ -band ID co-spatial with the compact radio source. This was initially thought to be a hot-spot associated with a larger source. However, the imaging data presented in this paper suggest that it is indeed a discrete source, although a triple source spanning  $\sim 14$  arcmin cannot be ruled out completely (but see Jarvis et al. 2001).

**6C\*0201+499** ( $z = 1.981$ ) The  $K$ -band ID for this source is coincident with the southern lobe, although the small angular size of this source ( $\theta \approx 1$  arcsec) means that astrometric uncertainties could easily place the ID at the centre of the lobes.

**6C\*0202+478** ( $z = 1.613?$ ) The ID (a) for this source is in close proximity to two bright stars. The ID is faint at the position of the weak radio emission, between the two radio lobes, which we now take to include the core.

**6C\*0208+344** ( $z = 1.920$ ) We find a very faint  $K$ -band identification at the position of the southern radio component, although there are no indications from the radio data that this has a flat spectrum.

**6C\*0209+276** ( $z = 1.141?$ ) Our 4.9 GHz radio map barely resolves this source. We do find a bright  $K$ -band identification at the position of the radio source, its magnitude suggests that our tentative redshift of  $z = 1.141$  is correct.

#### 4 THE $K-z$ HUBBLE DIAGRAM

In this section we compare the infrared Hubble diagram for the 6C\* sources with previous flux-density-limited samples, namely the 3CRR sample and 6CE sample along with data from the 7C-III sample (Lacy et al. 2000). The 3CRR (6CE) sample has a flux-density limit a factor of about twelve (two) brighter than 6C\*, this range allows us to break the strong biases inherent in flux-density limited samples (e.g. Blundell et al. 1999). The  $K$ -band magnitudes for the 3CRR sample have been compiled from the literature, the majority from the work of Lilly & Longair (1984). Other sources of 3CRR  $K$ -band magnitudes are Best, Longair & Röttgering (1998) and de Vries et al. (1998). These data are complemented by the virtually spectroscopically complete 6CE sample. The  $K$ -band magnitudes for this sample have been gathered from the literature, mainly from Eales et al. (1997) and Eales & Rawlings (1996). There are five sources from the 6C\* sample which are omitted from the  $K - z$  analysis: these are the two broad line quasars (6C\*0052+471 and 6C\*0154+450) where the  $K$ -band light may be dominated by emission from the quasar nucleus, 6C\*0139+344 which may have a foreground galaxy contributing to its  $K$ -band flux, 6C\*0155+424 as this looks like a merger system and the radio source ID is uncertain and 6C\*0202+478 which is in too close proximity to a star to measure accurate photometry. This source is also one of the sources with an uncertain redshift, thus there are only five filled stars in Figs. 3 & 4.

##### 4.1 Correcting to a metric aperture

A problem when comparing broad-band magnitudes for objects over a large redshift baseline is that the magnitudes cannot be measured in an aperture of a given physical diameter, if the redshift is unknown. If the redshift is known then the angular diameter can then be adjusted to correspond to a metric aperture of a given physical size for all of the sources. However, we do not

have the  $K$ -band images for the sources in the 3CRR and 6CE samples available for re-measuring the photometry in a single metric aperture. Therefore, we need a method of converting from our broad-band magnitudes measured in a specific angular aperture to our chosen metric aperture. To correct to a metric aperture, we follow the prescription of Eales et al. (1997), where the metric aperture used is 63.9 kpc, which corresponds to an angular size of  $\approx 8$  arcsec at  $z \geq 1$ . For the low-redshift ( $z < 0.6$ ) sources we use the curve of growth analysis of Sandage (1972), because at these redshifts the radio galaxies are predominantly associated with giant ellipticals (e.g. Rogstad & Ekers 1969). At high redshift ( $z > 0.6$ ) we use a power-law intensity profile of the form  $I \propto r^\alpha$  where we use  $\alpha = 0.35$ , the value derived by Eales et al. (1997).

##### 4.2 Emission-line contamination of $K$ -band magnitudes

The emission-line contamination of the measured continuum magnitudes for our dataset also needs to be accounted for, especially for the most-luminous sources at high redshift, where the bright optical emission lines are redshifted into the infrared.

To subtract this contribution we use the correlation between [OII] emission-line luminosity  $L_{\text{[OII]}}$  and the low-frequency radio luminosity  $L_{151}$  from Willott (2000), where  $L_{\text{[OII]}} \propto L_{151}^{1.00 \pm 0.04}$ . Thus, for a source with a given  $L_{151}$  we can estimate  $L_{\text{[OII]}}$ . Then by using the emission-line flux ratios for radio galaxies from McCarthy (1993) for emission lines below 5007Å, and from Robinson et al. (1987), Ward et al. (1991) and Rudy et al. (1992) for the longer wavelength emission lines, we are able to determine the contribution to the  $K$ -band magnitude from all of the other emission-lines. Assuming a square transmission window centred at  $2.2\mu\text{m}$  with a width of  $0.48\mu\text{m}$ , and a flux-density of  $4.07 \times 10^{-14} \text{ W m}^{-2} \text{ Å}^{-1}$  corresponding to a zeroth magnitude star in the  $K$ -band (Longair 1992), we convert this flux-density to a  $K$ -magnitude. In Fig. 2 we show the emission-line contamination to the  $K$ -band magnitude for various radio flux-densities over the redshift range  $0.0 < z < 10$ . The total emission-line contribution to the  $K$ -band flux is subtracted from the measured  $K$ -band flux and the remaining flux should be due to the stellar continuum. This assumes that there is no other contribution from the non-stellar continuum such as reddened and/or scattered quasar light (e.g. Simpson, Rawlings & Lacy 1999; Leyshon & Eales 1998).

Fig. 3 shows the emission-line corrected  $K - z$  diagram for the objects in our dataset. To analyse the differences between samples at low and high redshifts we split the data into three redshift bins. The low-redshift bin ( $z < 0.6$ ) is the low-redshift bin chosen by Eales et al. (1997), and is the redshift above which the alignment effect is seen (McCarthy 1993). The medium-redshift

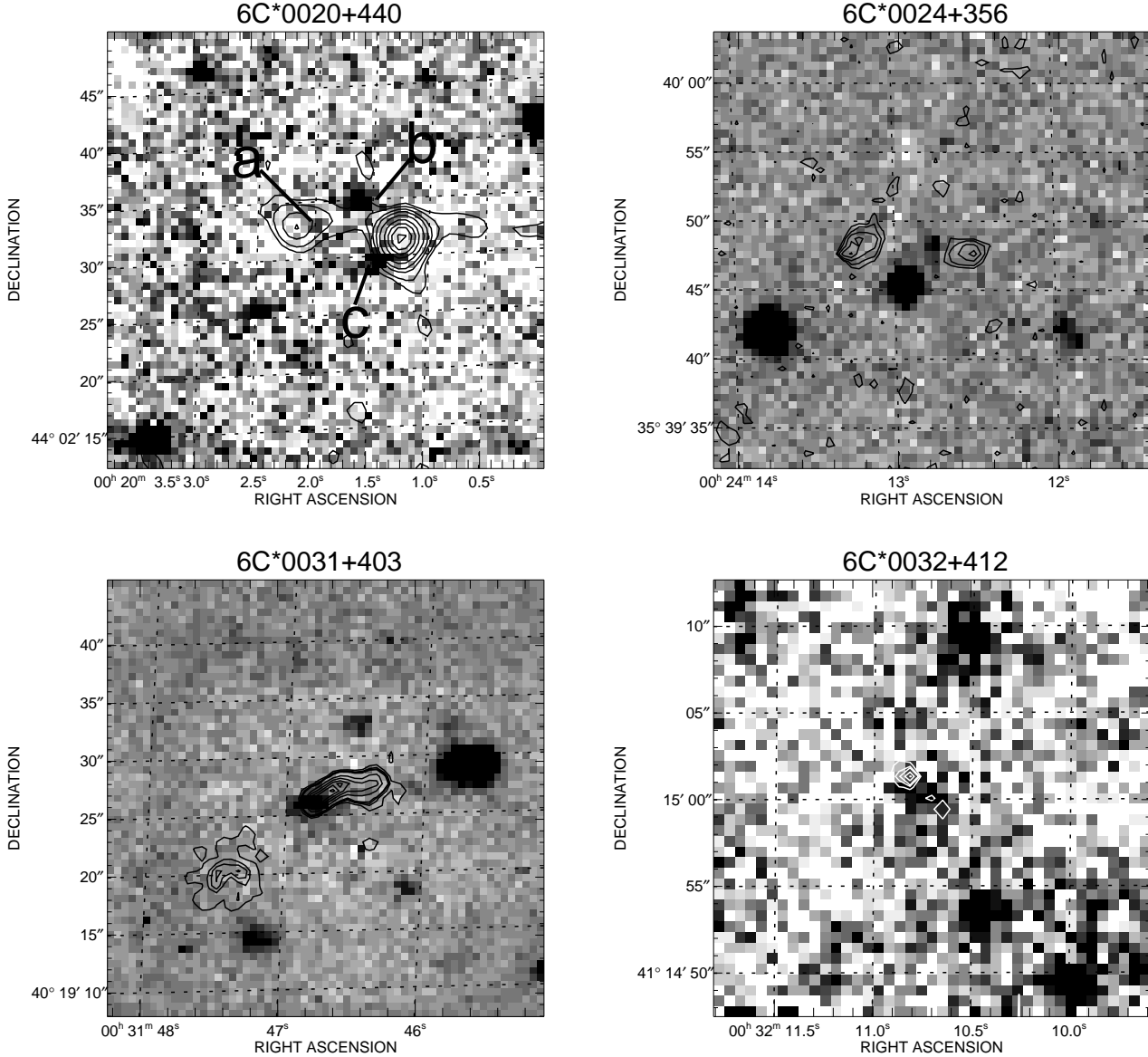
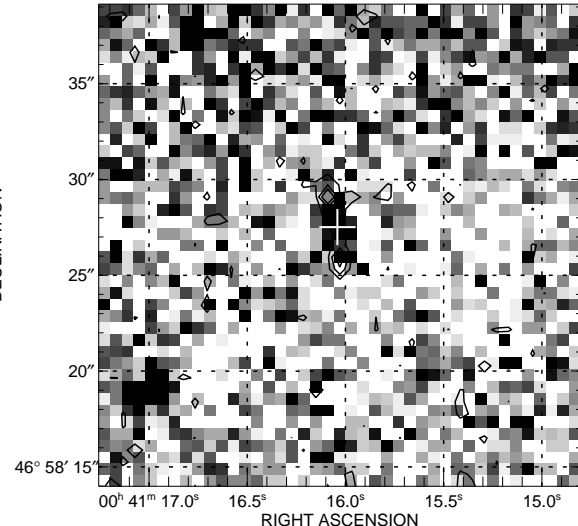


Figure 1:  $K$ -band images (greyscale) of 28 6C\* sources, with the radio contours overlaid. A detailed account of the radio galaxy 6C\*0140+326 can be found in Rawlings et al. (1996) and a deep near-infrared image in van Breugel et al. (1998). The coordinates are in B1950 and the frequency of the radio contours are those presented in Blundell et al. (1998) except where otherwise stated. For presentation purposes the images obtained in 1997 have all been binned up by averaging over  $2 \times 2$  pixels to produce roughly the same pixel scale as the 1993 and 1994 exposures. Likewise the images taken in 2000 have been binned up by averaging over  $3 \times 3$  pixels, this produces a slightly smaller pixel scale than for the other observations. For the images of 6C\*0050+419, 6C\*0106+397 and 6C\*0132+330 these have also been smoothed by a Gaussian with  $\sigma = 1$  pixel to make the ID clearer. For the images where the radio contours are not visible due to the scale of the optical ID encompassing most of the radio contours we have marked the peak of the radio emission with a white cross. There was a flat-fielding problem for the image of 6C\*0154+450, which is apparent towards the north-east of the image but this does not affect the magnitude given in Table 2. The  $K$ -band images and overlays of the sources now excluded from 6C\* are presented in Appendix B.

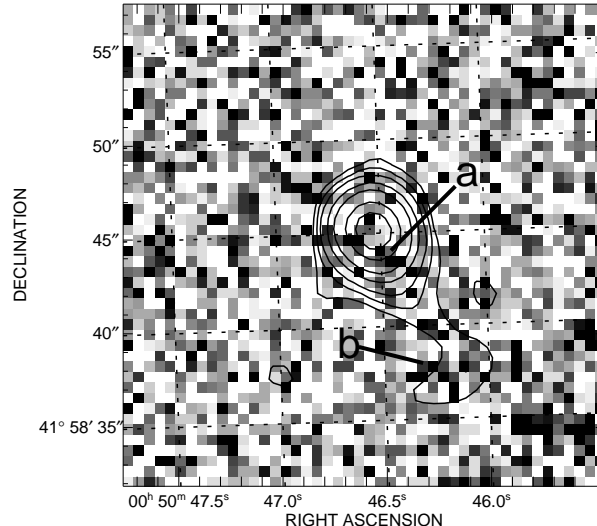
bin ( $0.6 < z < 1.8$ ) was chosen to enable us to directly compare the 3CRR and 6CE objects which have the same redshift but vastly different radio luminosities. This bin also contains nine objects from 6C\* at

the lower radio flux-density of  $0.96 \leq S_{151} \leq 2.00$  Jy. The high-redshift bin ( $z > 1.8$ ) contains ten 6CE source and fifteen 6C\* objects. We also add seven objects from

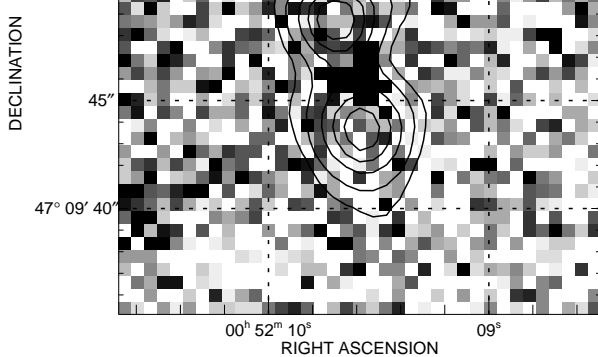
6C\*0041+469



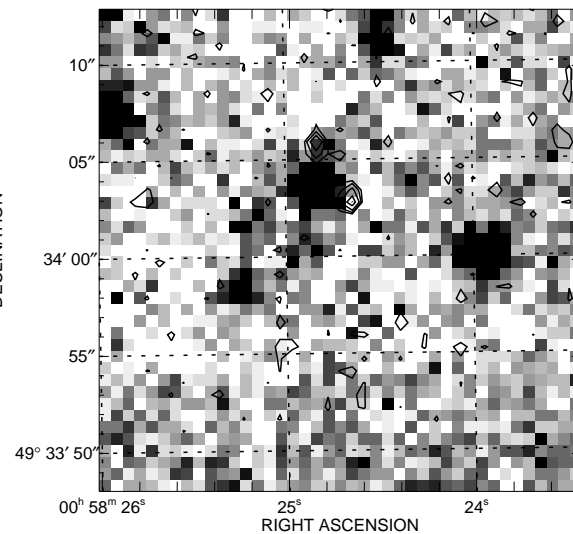
6C\*0050+419



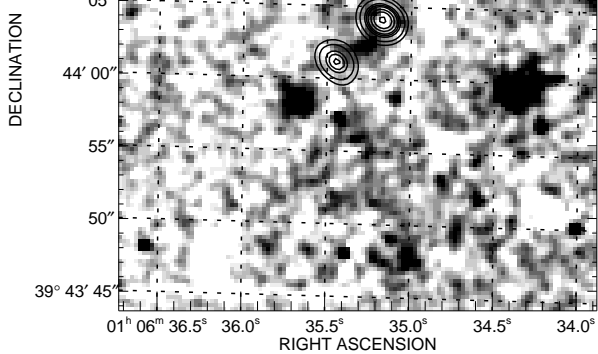
6C\*0052+471



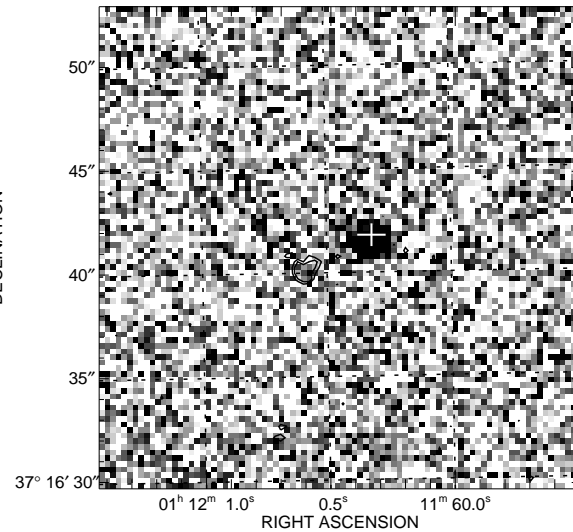
6C\*0058+495

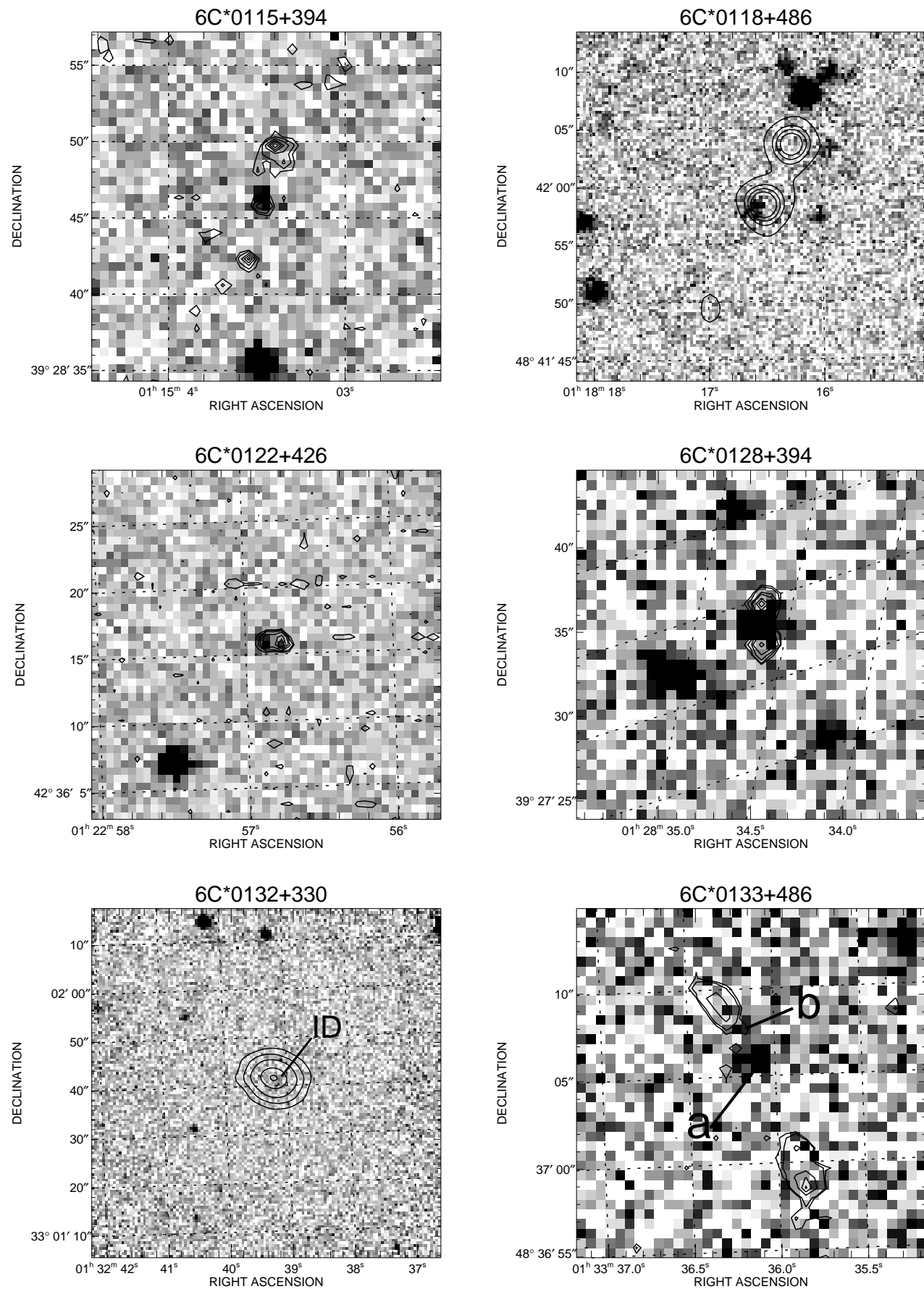


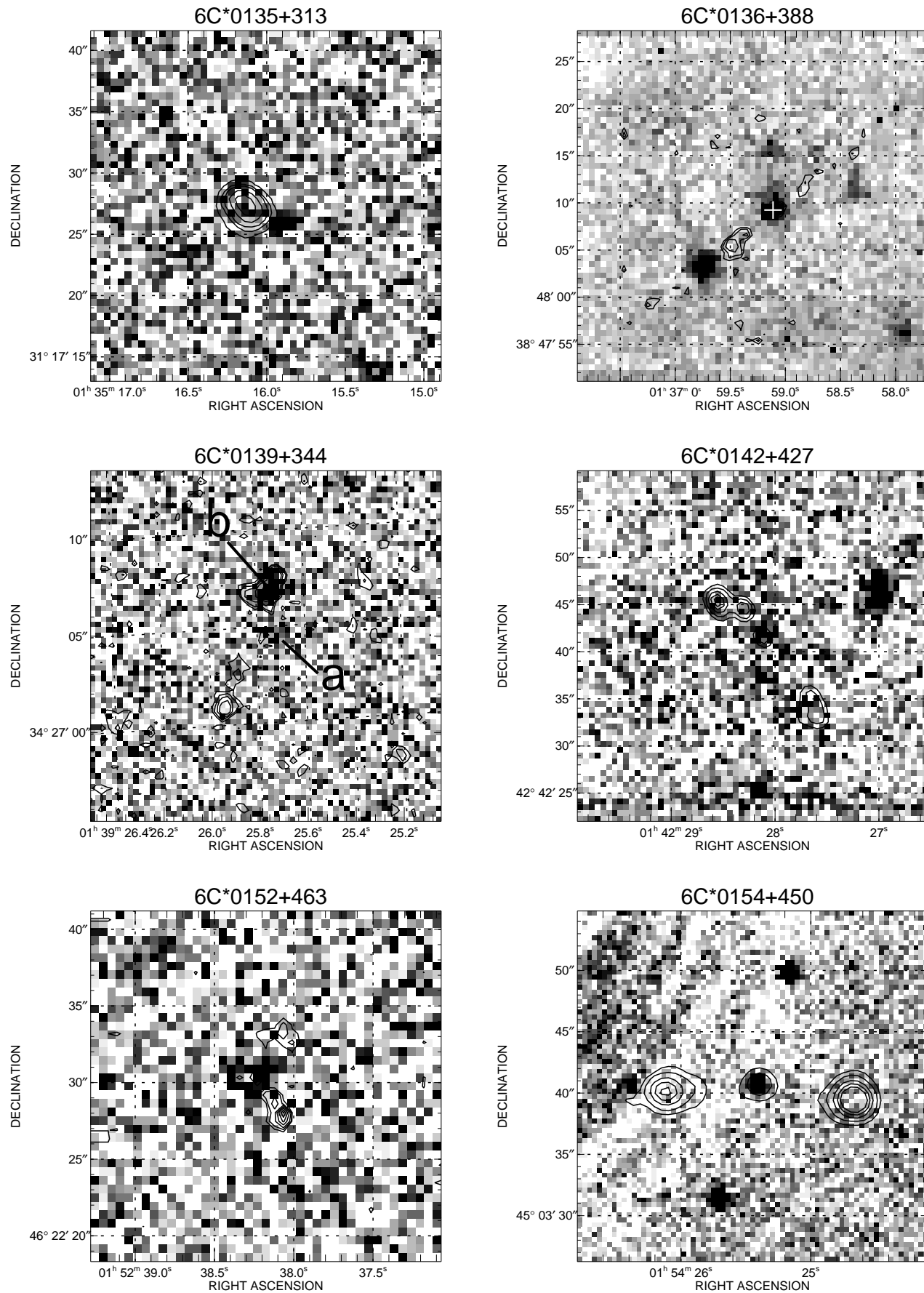
6C\*0106+397

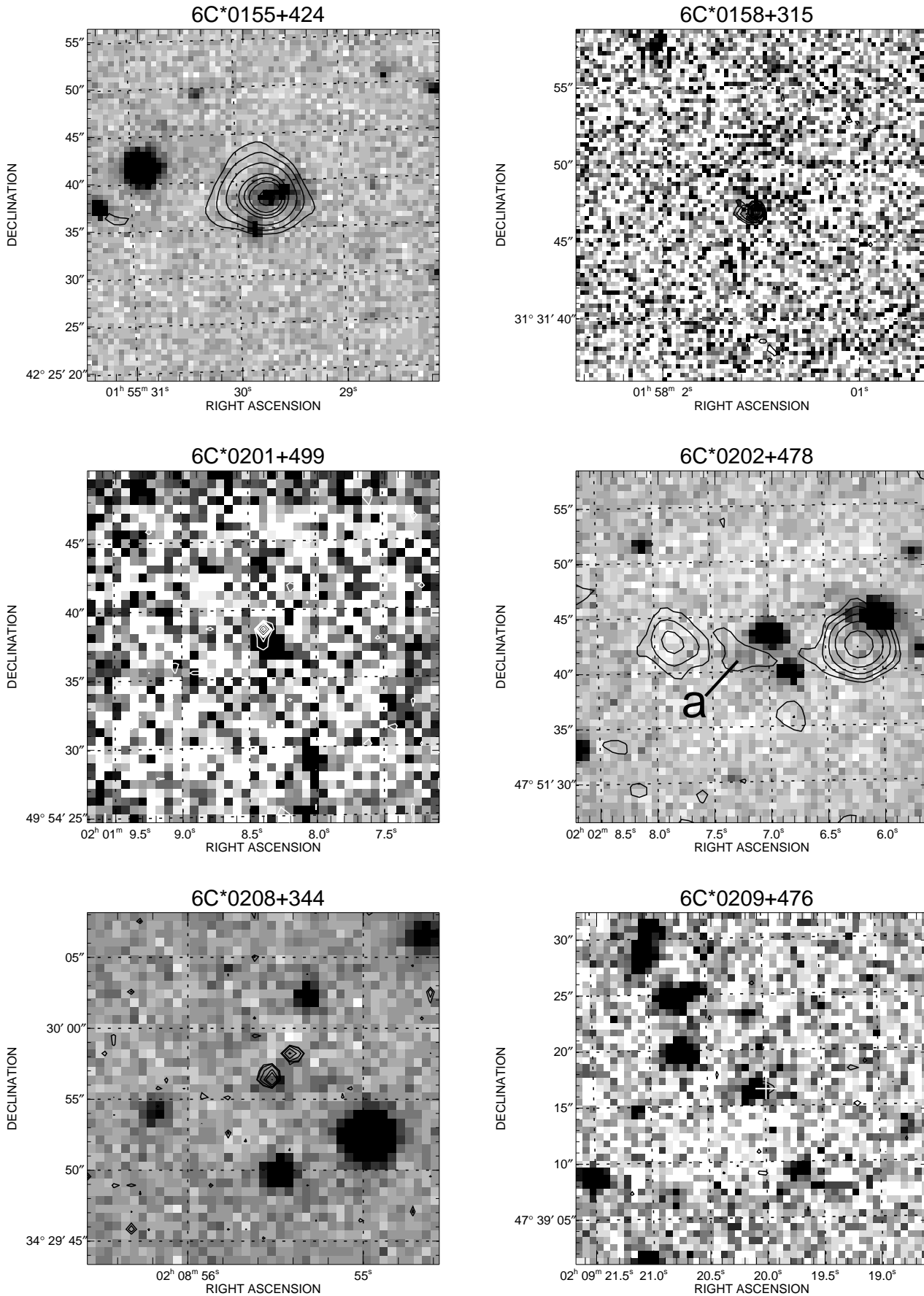


6C\*0112+372









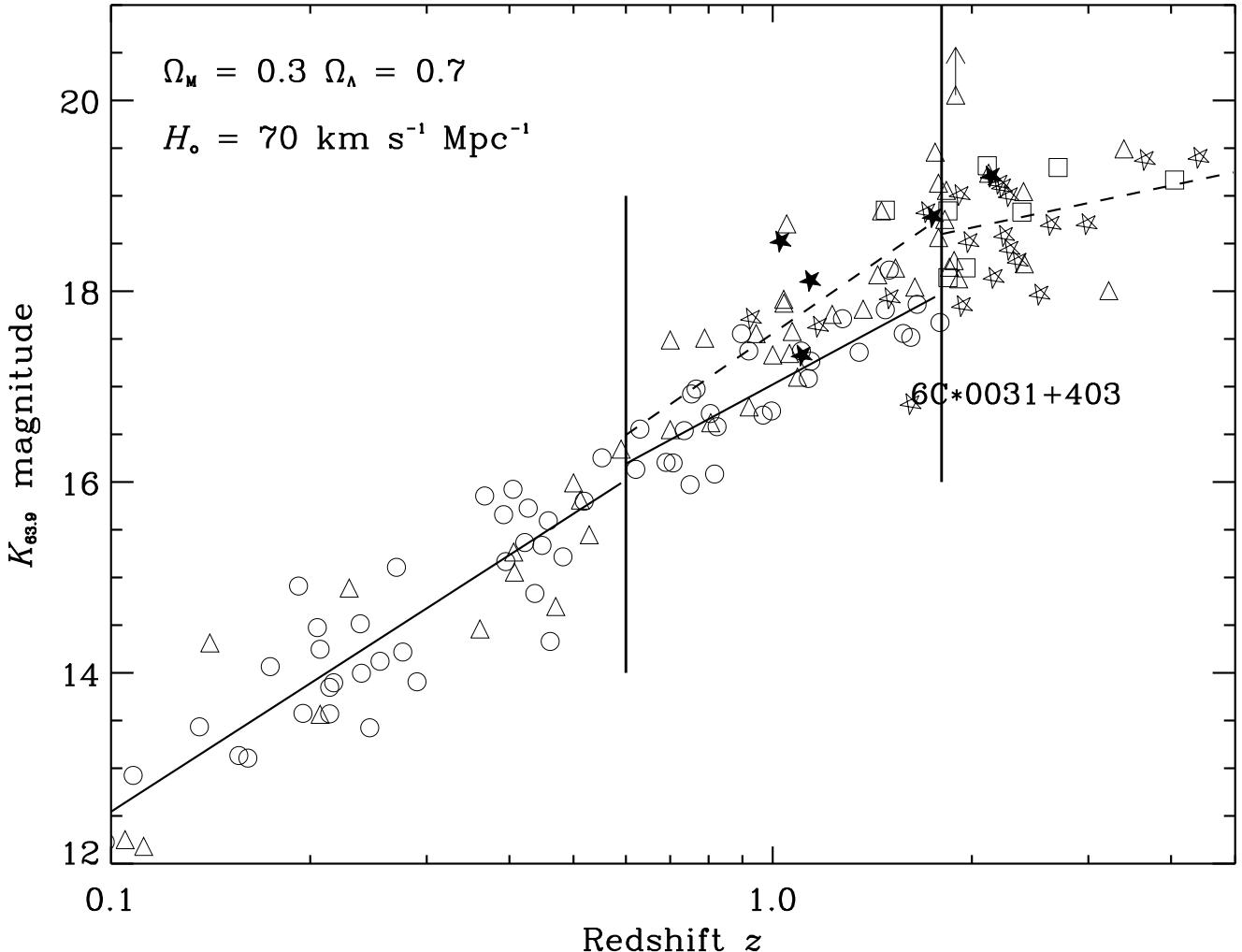


Figure 3: The  $K - z$  Hubble diagram for radio galaxies from the 3CRR (circles), 6CE (triangles), 6C\* (stars) and 7C-III (squares) samples, for a  $\Omega_M = 0.3$ ,  $\Omega_\Lambda = 0.7$  cosmology with  $H_0 = 70 \text{ km s}^{-1} \text{ Mpc}^{-1}$ , in line with the recent observational evidence (e.g. Perlmutter et al. 1999; Balbi et al. 2000; Gibson & Stetson 2001).  $K_{63.9}$  denotes the  $K$ -band magnitude within a metric aperture of 63.9 kpc (c.f. Eales et al. 1997), and all magnitudes have been corrected for emission-lines following the prescription given in Sec. 4.2. The two vertical lines show the redshift above which the alignment effect begins to be seen ( $z = 0.6$ ) and the higher redshift at which we chose to split the data and beyond which there are zero 3CRR sources ( $z = 1.8$ ). The solid lines are the fits to the 3CRR data points at  $z < 0.6$  and  $0.6 < z < 1.8$ . The dashed line is the fit to the 6CE and 6C\* sources at  $0.6 < z < 1.8$  and  $z > 1.8$ . 6C\*0031+403 probably has an AGN component contributing to the  $K$ -band magnitude (Sec. 3) and is labelled. The filled stars represent five of the six objects in 6C\* which do not yet have completely secure redshifts.

the 7C-III sample from Lacy et al. (2000) to the high-redshift bin.

## 5 GALAXY EVOLUTION AND THE FORMATION EPOCH

### 5.1 Dispersion in the $K - z$ diagram

We now calculate the residuals in  $K$ -band magnitude from straight line fits (calculated by minimising the square of the residuals in magnitude) to various subsets of the data in the three redshift bins considered

by Eales et al. (1997),  $z < 0.6$ ,  $0.6 < z < 1.8$  and  $z > 1.8$ . To avoid the possibility of confusing an increase in the dispersion in the data with the correlation between  $L_{151}$  and the  $K$ -band magnitude (c.f. Dunlop & Peacock 1993; Eales et al. 1997) we fit separate straight lines to the 3CRR data points and to the 6CE and 6C\* data points which we consider together due to their similar flux-density limits. For the following sections concerning the  $K - z$  diagram we also switch to the currently favoured cosmology of  $\Omega_M = 0.3$  and  $\Omega_\Lambda = 0.7$  with  $H_0 = 70 \text{ km s}^{-1} \text{ Mpc}^{-1}$ . Although this choice does not affect the dispersion calculated in this

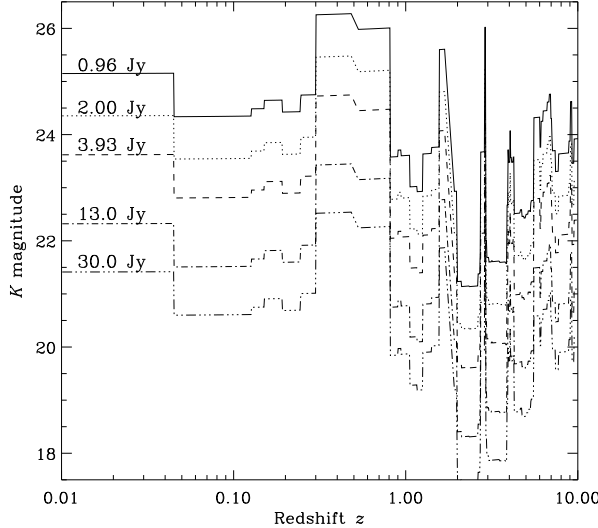


Figure 2: Emission line contribution to the  $K$ -band magnitudes for various radio flux-densities assuming the power-law relation of  $L_{\text{[OII]}} \propto L_{151}^{1.00}$ . The troughs in the plot occur where bright emission lines are redshifted into the  $K$ -band transmission window. For the samples used in this paper, the 3CRR sample is the dominant contributor of sources at  $z < 1.8$  and thus the 13 Jy line through the plot is an estimate of the minimum contribution from emission lines to the  $K$ -band flux. At  $z > 2$  the 6CE and 6C\* samples dominate and as such the upper three lines from 3.93 Jy to 0.96 Jy demonstrate the typical contribution from emission lines at these redshifts.

section (as all of the magnitudes have been adjusted to the chosen metric aperture in this cosmology), it does affect the results presented in Sec. 5.2 where synthetic spectral libraries are used to generate the expected path through the  $K - z$  diagram for various star-formation histories.

For the low-redshift sources in the 3CRR sample, we find that the dispersion about the fitted line has a standard deviation of  $\sigma = 0.52$ . Repeating this for the 6CE sources at  $z < 0.6$  we find that the standard deviation is slightly higher with  $\sigma = 0.57$ . The  $F$ -variance test for these distributions shows that they are statistically indistinguishable, with a significance of  $\sim 72\%$  that they are drawn from different distributions, agreeing with the results of Eales et al. (1997).

At higher redshift we find that the standard deviation of the residuals in  $K$ -band magnitude for 3CRR sources at medium redshift ( $0.6 < z < 1.8$ ) is  $\sigma = 0.36$ . The  $F$ -variance test shows that the difference in dispersion between the low- and medium-redshift 3CRR bins are significantly different at the 97% level. Hence, we find less scatter between  $0.6 < z < 1.8$  than at  $z < 0.6$  for the 3CRR sources in our sample. This can be explained in two ways. First, if there is a radio luminosity dependent component other than emission-lines, con-

tributing to the  $K$ -band flux, then the lower luminosity host galaxies will be more affected than the hosts with higher luminosities galaxies. Consequently the spread in observed magnitude becomes tighter, however this contribution would have to be significant ( $> 30\%$ ) and the observational evidence suggests that this is not the case at least at  $z \sim 1$  (e.g. Leyshon & Eales 1998; Simpson et al. 1999). Second, we know that the 3CRR galaxies in this redshift bin are the most extreme radio luminous sources in the universe. Therefore, we would expect them to harbour the most massive black holes, formation of which probably requires very tight physical conditions intrinsically linked to the host galaxy. Thus, the tightness of the  $K - z$  relation for 3CRR sources in the mid-redshift bin may be providing an insight into the physical conditions needed to form the most massive black holes and consequently the most luminous radio galaxies, whereas lower-luminosity radio galaxies with lower-mass black holes could possibly form in galaxies with a range of properties and environments, thus the dispersion is higher.

For the medium-redshift 6CE and 6C\* points we find that the standard deviation of the 6CE and 6C\* sources about the fitted line has a value of  $\sigma = 0.59$  ( $\sigma = 0.55$  if the sources with uncertain redshifts are omitted from the analysis), compared to  $\sigma = 0.57$  for the low-redshift 6CE sources and  $\sigma = 0.36$  for the medium-redshift 3CRR sources. Therefore the dispersion in the medium-redshift 6CE sources is similar to that at low-redshifts, whereas there is significant difference (confidence  $> 97\%$ ) between the 3CRR and 6CE/6C\* sources at medium redshifts. This may be explained by both of the points made earlier to the lower-luminosity 6CE/6C\* sources. The range in host galaxy properties could now span a very wide range while still harbouring a massive black hole and the radio luminosity is so much lower that any near-infrared component linked to the luminosity of the radio emission will be much weaker.

We now repeat this analysis for the high-redshift ( $z > 1.8$ ) points. As there are no 3CRR points above  $z = 1.8$  we only compare the residuals of the 6CE and 6C\* points in the medium- and high-redshift bins. The standard deviation in the high-redshift bin is  $\sigma = 0.51$  (exclusion of the sources with uncertain redshifts does not alter this value) compared to  $\sigma = 0.59$  in the medium-redshift bin. These are statistically indistinguishable with the  $F$ -variance test showing that the variances are different at the 40% significance level. It is also worth noting that there is no significant difference in the normalisation of the fitted line or in the dispersion of the 6CE sources and 6C\* sources at any redshift. Thus, there is no detectable difference between the two samples.

Therefore, unlike the results of Eales et al. (1997) we find no evidence of an increase in the dispersion in the  $K$ -band magnitudes from  $z < 2$  to  $z > 2$ . Lacy

et al. (2000) also find that the dispersion in luminosities of the hosts radio galaxies increases towards high redshift. They find a standard deviation of  $\sigma = 0.53$  in the medium-redshift bin. However, in their high-redshift bin they find that the standard deviation increases to  $\sigma = 0.93$ . This difference cannot be explained by accounting for the emission-line contribution as Lacy et al. also compensated for this. One possible effect that we have neglected is any non-stellar emission, which is not in the form of emission lines, which was addressed by Lacy et al. (2000). However, any additional luminosity dependent contribution would also affect the results of Eales et al. (1997) in the same way, and it would need to be considerable to make the dispersion of the medium- and high-redshift distributions significantly different. Thus the lack of sources at  $z > 1.8$  in the work of Eales et al. (1997) and Lacy et al. (2000) may be playing the dominant rôle in their determination of the dispersion at high redshift. Therefore, we conclude that there is no evidence from our data of an increase in the scatter in the  $K - z$  diagram from  $z \sim 0.6$  to  $z \sim 3$  for the 6CE/6C\* sources.

## 5.2 The $K - z$ diagram and evolutionary models

In this section we compare our  $K - z$  diagram for radio sources from the 3CRR, 6CE, 7C-III and 6C\* radio samples with previous results in the literature and the galaxy evolution models of Bruzual & Charlot (1993).

Eales et al. (1997) found that in an  $\Omega_M = 1$  universe with  $\Omega_\Lambda = 0$ , the hosts of radio galaxies in the 6CE sample were consistent with a non-evolving population for  $z < 2$ . However, for a low-density universe ( $\Omega_M = 0$ ) the  $K - z$  diagram for the 6CE sample becomes consistent with a passively evolving population to  $z \sim 2$ . Beyond  $z > 2$  the radio galaxies are systematically brighter than the no-evolution model and the passive evolution curves in both cosmologies considered. Eales et al. (1997) used this as evidence that we are probing the epoch of galaxy formation at  $z \gtrsim 2$ . Using high-redshift radio galaxies from a number of flux-density-limited radio samples, van Breugel et al. (1998) find that the near-infrared colours of radio galaxies at  $z > 3$  are very blue, consistent with a young stellar population. They also suggest that the size of the near-IR emission regions at  $z > 3$  are comparable with the size of the radio structures, with the near-IR component also more aligned with the radio components at  $z > 3$  than at  $z < 3$ . This suggests an intrinsic link between the star-formation activity and the radio emission at high-redshift, with these two processes probably triggered at roughly the same time by the same mechanism. Lacy et al. (2000) using the flux-density-limited 7C-III radio sample find evidence that the hosts of radio-loud galaxies become more luminous with redshift, consistent with a passively evolving population which formed at high-redshift ( $z > 3$ ). Thus, all of the evidence suggests that

radio galaxies at  $z \lesssim 3$  are associated with host galaxies which formed the bulk of their stellar populations at epochs corresponding to  $z \gtrsim 3$  and which have undergone simple passive stellar evolution from the time the bulk of their stars formed to the time at which they develop the jets we see (although non-stellar contamination may mean this inference from  $K$ -band magnitudes is not yet firm).

In Fig. 4 we plot the  $K - z$  diagram for all of the sources in our dataset. We also show four synthetic galaxy evolution models from the ‘Galaxy Isochrone Synthesis Spectral Evolution Library’ (GISSEL) of Bruzual & Charlot (1993) and a curve representing a galaxy which undergoes no-evolution. The GISSEL files that we have used are ones in which there is an instantaneous burst of star formation and one in which the burst of star formation lasts 1 Gyr, with a Salpeter IMF with a lower mass cut-off of  $0.1 M_\odot$  and an upper mass cut-off of  $125 M_\odot$ . We use two different assumptions about the star formation history, one in which the burst of star formation begins at  $z = 5$  and one in which the burst occurs at  $z = 10$ .

The no-evolution curve was constructed by taking the spectral energy distribution template from the GISSEL library, that was found to fit the observed spectral energy distribution of a radio galaxy at  $z = 0$ , and which also reproduced the near-infrared colours. All of the curves are normalised to pass through the low-redshift ( $z < 0.3$ ) points.

With our data on the 6C\* sample in addition to the 6CE and 7C-III samples we find that in a low-density universe ( $\Omega_M = 0.3$  and  $\Omega_\Lambda = 0.7$ ) the data are predominantly brighter than the no-evolution curve and are consistent with a passively evolving stellar population with a high-formation redshift. If this passively evolving scenario is correct then hierarchical growth at  $z < 2.5$  is not a required ingredient. However, this brightening may not just be due to passive evolution of the stellar population. Non-stellar contributions from the central AGN may also contribute a higher fraction of light at these redshifts. All of the studies to measure the non-stellar contribution to the  $K$ -band flux conducted to date (e.g. Leyshon & Eales 1998; Simpson, Rawlings & Lacy 1999), have concentrated on the most radio luminous 3CR sources at  $z \simeq 1$ , and may have little bearing on the properties of the high-redshift sources considered in this paper. If it turns out that the high-redshift 6C sources have  $\gtrsim$  non-stellar contamination to those of the  $z \sim 1$  3C sources (which have the same radio luminosity) then hierarchical build up may be necessary. Note that  $K$ -band observations of the high-redshift 6C sources will be at shorter wavelengths than those of the 3C sources.

However, separate arguments lead us to conclude that the dominant factor is passive evolution of a stellar population which formed at  $z \gtrsim 2.5$ . First, recent sub-mm observations with SCUBA have shown that the

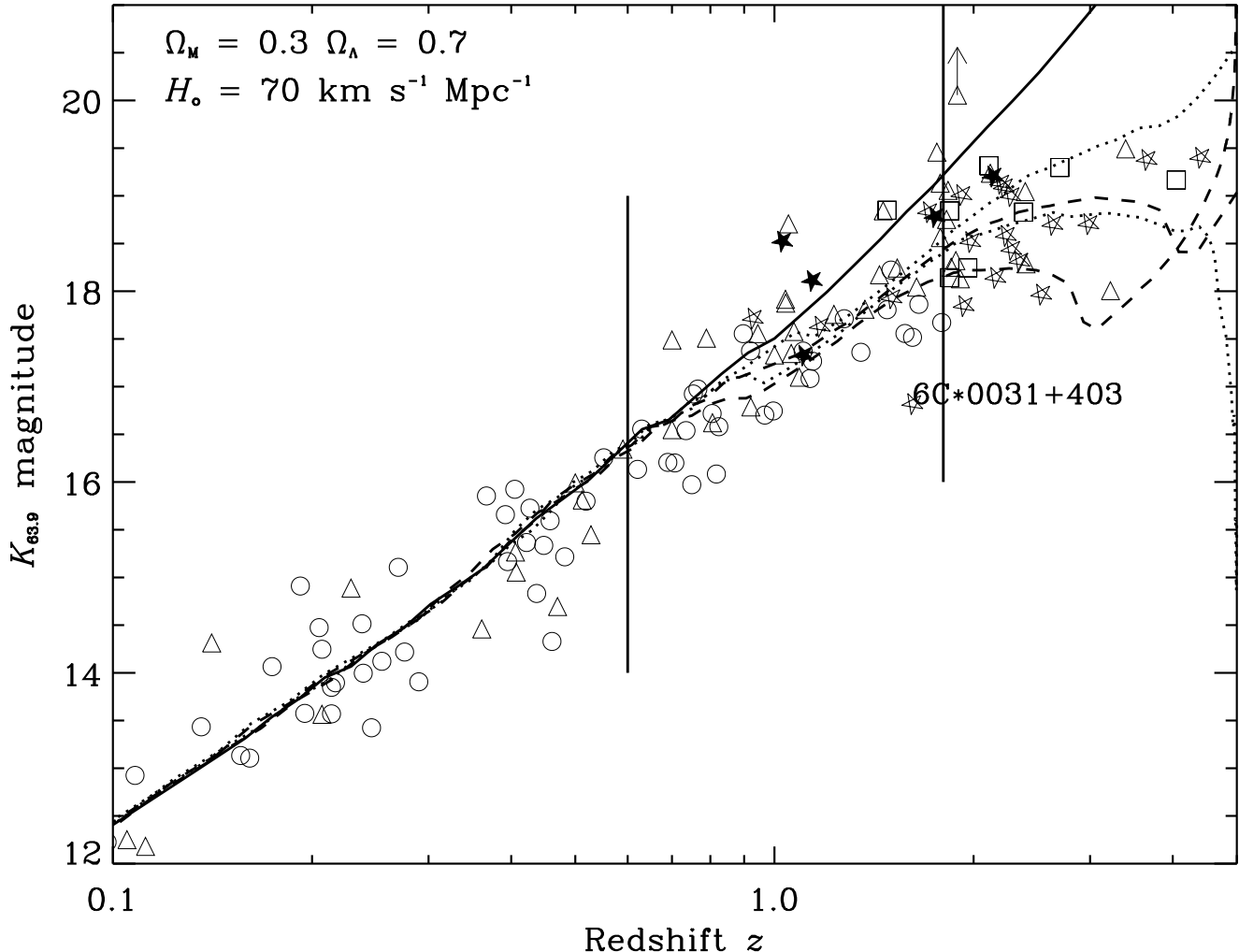


Figure 4: The  $K - z$  Hubble diagram for 3CRR, 6CE and 6C\* radio galaxies as defined in Fig 3. The two vertical lines show the redshift above which the alignment effect begins to be seen ( $z > 0.6$ ) and the higher redshift at which we chose to split the data ( $z = 1.8$ ). The solid curved line is the predicted curve for galaxies which do not evolve (as described in the text). The dashed line is the model for a star-burst lasting 1 Gyr starting at  $z = 5$  and the dotted curve is the same evolutionary model but with the same starburst beginning at  $z = 10$ . The two dotted curves represent the models of an instantaneous (0.1 Gyr) burst beginning at  $z = 5$  (lower) and  $z = 10$  (upper).

dust masses in radio galaxies are larger at  $z \simeq 3$  than in galaxies with similar radio luminosities at lower redshift (Archibald et al. 2001). This implies that the majority of star-formation activity in these galaxies is occurring at high redshift. Second, the discovery of six extremely red objects at  $1 < z < 2$  in the 7C Redshift Survey (Willott, Rawlings & Blundell 2001) with inferred ages of a few Gyrs, implies that these objects formed the bulk of their stellar population at  $z \simeq 5$ . Third, detailed modelling of the optical spectrum of the weak radio source LBDS 53W091 at  $z = 1.552$  has shown that this object is most plausibly an old elliptical, with an inferred age of  $\gtrsim 3.5$  Gyr (Dunlop et al. 1996; Spinrad et al. 1997). The further discovery of LBDS 53W069 at  $z = 1.43$ , with an inferred age of  $\sim 4$  Gyr (Dunlop 1999) suggests that there exists a population of evolved, radio weak

ellipticals which formed at  $z \gtrsim 5$ . However, controversy has arisen regarding these inferred ages with more than one group showing that alternative population synthesis models estimate these galaxies to be much younger, e.g. 1 - 2 Gyr (e.g. Bruzual & Magris 1997; Yi et al. 2000 - but see Nolan, Dunlop & Jimenez 2001), and this should be kept in mind. Fourth, Peacock et al. (1998) have presented an independent argument which corroborates the ages of these objects deduced from the gravitational collapse redshift required for consistency with the power spectrum which again leads to a high-formation redshift for these objects. Therefore, the new data on the 6C\* sample presented in this paper is consistent with the results from various other observational studies of radio galaxies in which these radio-luminous systems formed most of their stars at epochs corresponding to

very high redshifts ( $z \gtrsim 2.5$ ), and have undergone simple passive stellar evolution since. Willott et al. (2001) have pointed out that such galaxies probably undergo at least two active phases: one, at epochs corresponding to  $z \gtrsim 5$ , when the black hole and stellar spheroid formed, and another, at e.g.  $z \sim 2$ , when powerful jet activity is triggered, or perhaps re-triggered, by an event such as an interaction or a merger. The small scatter in the  $K - z$  relation (this paper) and sub-mm results (Archibald et al. 2001) suggest that the second active phase has little influence on the stellar mass of the final elliptical galaxy.

We have shown that the powerful radio galaxies in our samples are consistent with having passively evolving stellar populations. If we now compare the masses of these powerful radio galaxies to the derived value of  $M_K^*$  for nearby elliptical galaxies [ $M_K^* = -24.3$  for  $H_0 = 70 \text{ km s}^{-1} \text{ Mpc}^{-1}$  (Kochanek et al. 2000)], we find, if passive evolution is accounted for, that the powerful radio galaxies considered in this paper are consistent with being  $\approx 5L^*$  throughout the redshift range  $0 < z \lesssim 2.5$ .

## 6 CONCLUSIONS

We have obtained near-infrared images for the filtered 6C\* radio sample. With this filtered survey we are able to significantly increase coverage of the  $K - z$  Hubble diagram for radio galaxies at  $z > 2$  and have reached the following conclusions.

- 3CRR galaxies at  $z > 0.6$  show a tighter range in near-IR luminosity than at  $z < 0.6$ . This can be explained by a radio luminosity dependent component affecting the lower luminosity host galaxies more than the higher luminosity host galaxies, making the correlation tighter. Alternatively it may be a consequence of the small range of physical conditions needed to form the most massive black holes and hence the most luminous radio sources. With the addition of the fainter 6CE and 6C\* samples we find that the dispersion in  $K$ -band magnitude increases with decreasing radio luminosity, consistent with both of the above explanations.

- 6CE/6C\* galaxies at  $0.6 < z < 1.8$  have fainter  $K$ -band magnitudes than the 3CRR galaxies at similar redshifts, implying a link between radio luminosity and near-infrared luminosity, in agreement with earlier work (e.g. Dunlop & Peacock 1993; Eales et al. 1997). This may be a consequence of a link between radio luminosity/black hole mass and the mass of the host galaxy. The more massive galaxies harbour the most massive black holes, in accordance with recent work on nearby non-active galaxies (e.g. Magorrian et al. 1998).

- We find no evidence from our emission-line corrected  $K$ -band magnitudes for an increase in the dispersion of 6CE and 6C\* radio galaxies from  $z \sim 0.6$  to  $z \sim 2.5$ , indicating that we are not yet probing into the

epoch of formation in which we would expect to see a broader range in magnitudes.

- We find that radio galaxies are consistent with a passively evolving population which formed at high-redshift ( $z \gtrsim 2.5$ ), in agreement with recent sub-mm observations of radio galaxies (Archibald et al. 2001) and extremely red objects from the 7C Redshift Survey (Willott et al. 2001) and other faint radio surveys (e.g. Dunlop et al. 1996).
- The host galaxies of powerful radio galaxies appear to be associated with galaxies with a luminosity distribution with a high mean of  $\approx 5L^*$  and a low-dispersion ( $\sigma \sim 0.5$  mag) up to at least  $z \sim 2.5$ .

## ACKNOWLEDGEMENTS

We thank the many people involved in the acquisition of the imaging data on the 6C\* sample, and in particular, Jim Dunlop for obtaining the UKIRT image of 6C\*0032+412 and Paul Hirst for 6C\*0107+448. Hyron Spinrad, Daniel Stern, Arjun Dey and Adam Stanford who all helped with the Keck optical imaging observations. The United Kingdom Infrared Telescope is operated by the Joint Astronomy Centre on behalf of the U.K. Particle Physics and Astronomy Research Council. W.M.Keck Observatory is operated as a scientific partnership among the University of California, the California Institute of Technology, and the National Aeronautics and Space Administration. The Observatory was made possible by the generous financial support of the W.M.Keck Foundation.

## REFERENCES

Archibald E.N., Dunlop J.S., Hughes D.H., Rawlings S., Eales S.A., Ivison R.J., 2001, MNRAS, 323, 417  
 Balbi A., et al., 2000, ApJ, 545, 1  
 Best P.N., Longair M.S., Röttgering, 1997, MNRAS, 292, 758  
 Best P.N., Longair M.S., Röttgering, 1998, MNRAS, 295, 549  
 Blundell K.M., Rawlings S., Eales S.A., Taylor G.B., Bradley A.D., 1998, MNRAS, 295, 265 (paper I)  
 Blundell K.M., Rawlings S., Willott C.J., 1999, AJ, 117, 677  
 Bruzual G., Charlot S., 1993, ApJ, 405, 438  
 Bruzual G.A., Magris G.C., 1997, in The Ultraviolet Universe at Low and High Redshift, AIP vol.408 (AIP:Woodbury), 291  
 Chambers K.C., Miley G.K., van Breugel W.J.M., 1987, Nature, 329, 604  
 Condon J.J., Cotton W.D., Greisen E.W., Yin Q.F., Perley R.A., Taylor G.B., Broderick J.J., 1998, AJ, 115, 1693  
 Daly R.A., 1992, ApJ, 399, 426  
 de Vries W.H., O'Dea C.P., Perlman E., Baum S.A., Lehnert M.D., Stocke J., Rector T., Elston R., 1998, ApJ, 503, 138  
 Dunlop J.S., 1999, in 'The most distant radio galaxies' KNAW Colloquium, Amsterdam, October 1997, eds Röttgering et al., Kluwer  
 Dunlop J.S., Peacock J.A., 1993, MNRAS, 263, 936  
 Dunlop J.S., Peacock J.A., Spinrad H., Dey A., Jimenez R., Stern D., Windhorst R.A., 1996, Nature, 381, 581  
 Eales S.A., 1985, MNRAS, 217, 149  
 Eales S.A., Rawlings S., 1993, ApJ, 411, 67

Eales S.A., Rawlings S., 1996, ApJ, 460, 68  
 Eales S.A., Rawlings S., Law-Green D., Cotter G., Lacy M., 1997, MNRAS, 291, 593  
 Gibson B.K., Stetson P.B., 2001, ApJ, 547, 103  
 Hales S.E.G., Baldwin J.E., Warner P.J., 1993, MNRAS, 263, 25  
 Jarvis M.J., 2000, The Most Distant Radio Galaxies, PhD thesis, University of Oxford  
 Jarvis et al., 2001, MNRAS submitted (paper II)  
 Kochanek C.S., et al., 2000, ApJ, 543, 131  
 Lacy M., Bunker A.J., Ridgway S.E., AJ, 2000, 120, 68  
 Laing R.A., Riley J.M. & Longair M.S., 1983, MNRAS, 204, 151  
 Leyshon G., Eales S.A., 1998, MNRAS, 295, 10  
 Lilly S.J., 1989, ApJ, 340, 77  
 Lilly S.J., Longair M.S., 1984, MNRAS, 211, 833  
 Longair M.S., 1992, High Energy Astrophysics, Volume 1, Particles, photons and their detection 2nd edition, CUP  
 Magorrian J. et al., 1998, AJ, 115, 2285  
 McCarthy P.J., 1993, ARAA, 31, 639  
 McCarthy P.J., van Breugel W.J.M., Spinrad H., Djorgovski S.G., 1987, ApJL, 321, L29  
 McLure R.J., Dunlop J.S., 2000, MNRAS, 317, 249  
 Nolan L.A., Dunlop J.S., Jimenez R., 2001, MNRAS, 323, 385  
 Oke J.B. et al., 1995, PASP, 107, 375  
 Peacock J.A., Jimenez R., Dunlop J.S., Waddington I., Spinrad H., Stern D., Dey A., Windhorst R.A., 1998, MNRAS, 296, 1089  
 Perlmutter S. et al., 1999, ApJ, 517, 565  
 Rawlings S., Eales S.A., Lacy M., 2001, MNRAS, 322, 536  
 Rawlings S., Lacy M., Blundell K.M., Eales S.A., Bunker A.J., Garrington S.T., 1996, Nature, 383, 502  
 Rawlings S., Saunders R., 1991, Nature, 349, 138  
 Robinson A., Binette L., Fosbury R.A.E., Tadhunter C.N., 1987, MNRAS, 227, 97  
 Rogstad D.H., Ekers R.D., 1969, ApJ, 157, 481  
 Rudy R.J., Erwin P., Rossano G.S., Puetter R.C., 1992, ApJ, 384, 536  
 Sandage A., 1972, ApJ, 178, 25  
 Simpson C., Rawlings S., Lacy M., 1999, MNRAS, 306, 828  
 Spinrad H., Dey A., Stern D., Dunlop J., Peacock J., Jimenez R., Windhorst R., 1997, ApJ, 484, 581  
 Tadhunter C.N., Fosbury R.A.E., Binette L., Danziger I.J., Robinson A., 1987, Nature, 325, 504  
 van Breugel W.J.M., Stanford S.A., Spinrad H., Stern D., Graham J.R., 1998, ApJ, 502, 614  
 Ward M.J., Blanco P.R., Wilson A.S., Nishida M., 1991, ApJ, 382, 115  
 Willott C.J., 2000, to appear in AGN in their cosmic environment eds. B. Rocca-Volmerange and H. Sol  
 Willott C.J., Rawlings S., Blundell K.M., 2001, MNRAS in press (astro-ph/0104118)  
 Willott C.J., Rawlings S., Blundell K.M., Lacy M., 1999, MNRAS, 309, 1017  
 Yi S., Brown T., Heap S., Hubeny I., Landsman W., Lanz T., Sweigart A., 2000, ApJ, 533, 670

## APPENDIX A: *I*- BAND IMAGING FROM THE KECK TELESCOPE

In this appendix we present our Keck *I*— band images of 6C\*0041+460 and 6C\*0050+419. These images were obtained using LRIS (Oke et al. 1995) on the Keck-II telescope using a TEK 2048 × 2048 CCD detector with a pixel scale of 0.212 arcsec pixel<sup>-1</sup>.

## APPENDIX B: IMAGING DATA ON THE SOURCES EXCLUDED FROM THE 6C\* SAMPLE

In this appendix we show *K*-band and *R*-band images of the five sources which are now excluded from the 6C\* sample as more recent radio observations reveal that their angular sizes are larger than the cut-off value of 15 arcsec.

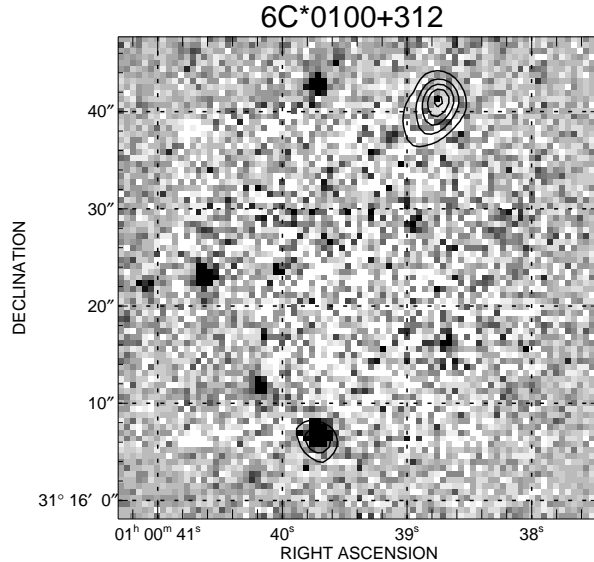


Figure 6: *K*-band image of the radio source 6C\*0100+312. The optical identification is unresolved and co-spatial with the core of the radio emission. There is also another lobe of radio emission, which is not shown on this image, to the south-east of the core at 01 00 41.20 +31 16 17.0 (B1950) which is co-linear with the core and the lobe to the north-west.

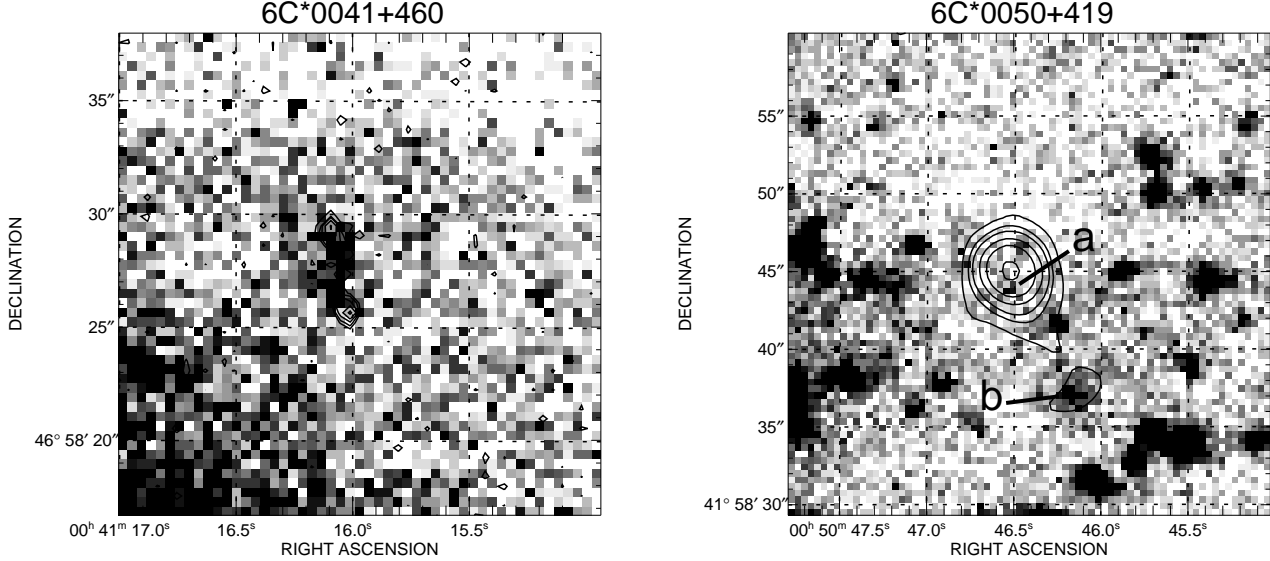


Figure 5: *I*-band images of the 6C\* radio sources 6C\*0041+460 (left) and 6C\*0050+419 (right) taken with the Keck-II telescope, with radio contours overlaid, the frequency of which are given in Table 2. The image of 6C\*0041+460 is a 300 second exposure and the ID has a magnitude of  $I = 23.51$  (8 arcsec aperture) and the *I*-band image has been shifted to the same astrometric frame as our *K*-band image (a shift of  $\approx 1$  arcsec east). The image of 6C\*0050+419 was a 450 second exposure and the magnitude of the probable ID associated with the faint radio emission to the south-west of the bright radio component (see Sec. 3) is  $I = 23.10$  (8 arcsec aperture).

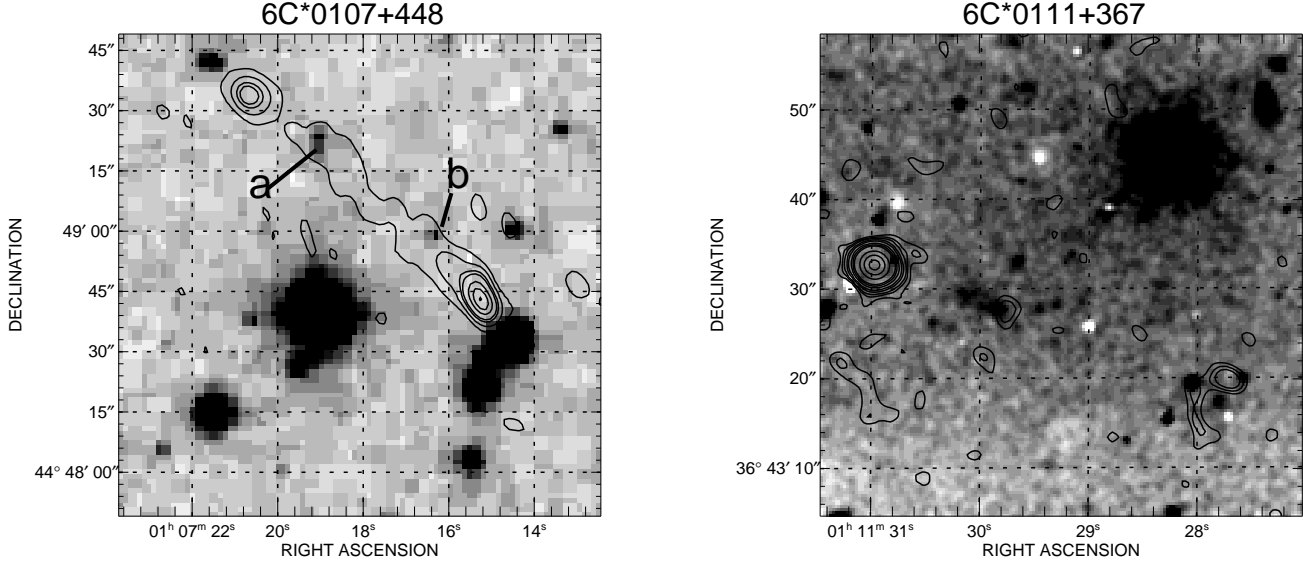


Figure 7: *R*-band digitised sky survey (DSS) image of 6C\*0107+448 overlaid with our new 1.4 GHz radio map (peak flux contour = 26 mJy/beam and the lowest contour = 1 mJy/beam). There are two possible optical counterparts for this radio source on the DSS image marked ‘a’ and ‘b’ on the image, with object ‘a’ being the most plausible ID. Our *K*-band image does not cover the area of sky containing the central region of this radio source.

Figure 8: WHT *R*-band image of 6C\*0111+367. The optical identification is (within the astrometric uncertainties) co-spatial with the central radio component in our 8.4 GHz map, with the two radio lobes co-linear with each other and the core, the image has been smoothed with a 2D Gaussian of  $\sigma = 1$  pixel for presentation purposes.

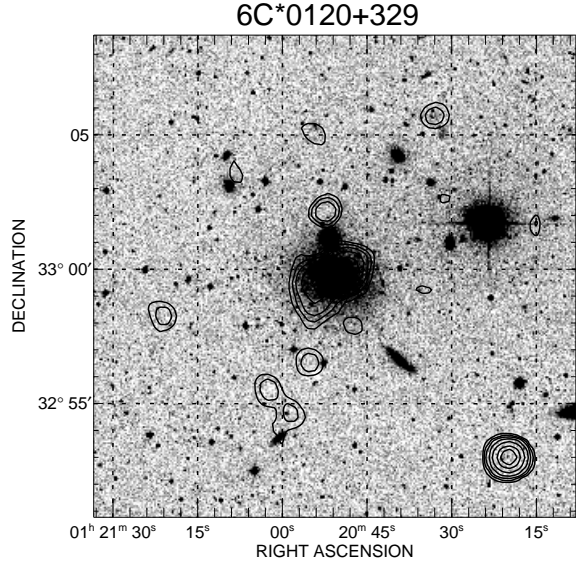


Figure 9: *R*-band DSS image of 6C\*0120+329. The 1.4 GHz NVSS (Condon et al. 1998) map shows there is a radio source associated with an extended galaxy at  $z = 0.0164$  (Jarvis et al. 2000).

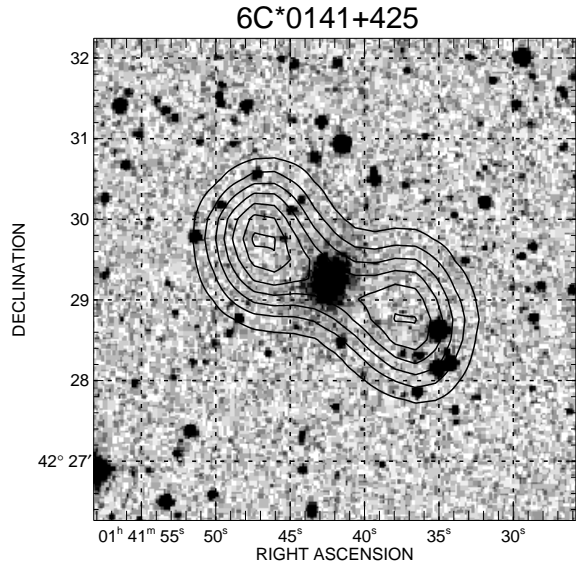


Figure 10: *R*-band DSS image of 6C\*0141+425 overlaid with the 1.4 GHz NVSS map. One can see the optical identification is co-spatial with the midpoint of the radio peaks.